Complexity and dynamics of *in organello* translation landscape assessed by high-resolution mitochondrial ribosome profiling

Taisei Wakigawa[1,2,7], Mari Mito[1,7], Haruna Yamashiro[1], Kotaro Tomuro[1,2], Haruna Tani[3], Kazuhito Tomizawa[4], Takeshi Chujo[4], Asuteka Nagao[5], Takeo Suzuki[5,6], Fan-Yan Wei[3], Yuichi Shichino[1], Tsutomu Suzuki[5], and Shintaro Iwasaki[1,2,8†]

[1]RNA Systems Biochemistry Laboratory, RIKEN Cluster for Pioneering Research, Wako, Saitama 351-0198, Japan

[2]Department of Computational Biology and Medical Sciences, Graduate School of Frontier Sciences, The University of Tokyo, Kashiwa, Chiba 277-8561, Japan

[3]Department of Modomics Biology and Medicine, Institute of Development, Aging and Cancer, Tohoku University, Sendai, Miyagi 980-8575, Japan

[4]Department of Molecular Physiology, Faculty of Life Sciences, Kumamoto University, Kumamoto, Kumamoto 860-8556, Japan

[5]Department of Chemistry and Biotechnology, Graduate School of Engineering, The University of Tokyo, Bunkyo-ku, Tokyo, 113-8656, Japan

[6]Department of Medical Biochemistry, Graduate School of Medicine, University of the Ryukyus, Nishihara, Okinawa 903-0215, Japan

[7]These authors contributed equally.

[8]Lead contact

[†]Correspondence should be addressed to S.I.

E-mail: shintaro.iwasaki@riken.jp

Abstract

Eukaryotes house an additional protein synthesis system within the mitochondria. Given that mitochondrial translation dictates OXPHOS complex abundance and ATP levels in cells, exhaustive, quantitative, and high-resolution delineation of mitoribosome traversal is needed. Here, we developed a technique for high-resolution mitochondrial ribosome profiling and unveiled the tight regulation of mammalian *in organello* translation. Our approach assessed the stoichiometry and kinetics of mitochondrial translation flux, such as the absolute numbers of mitoribosomes on a transcript and the elongation rate, initiation rate, and lifetime rounds of translation of individual transcripts. We also surveyed the impacts of modifications at anticodon stem loop in mt-tRNAs, including all possible decorations at 34th position, by deleting the corresponding enzymes and harnessing patient-derived mtDNA A3243G cells. Moreover, retapamulin-assisted profiling and disome profiling unveiled cryptic translation initiation sites at subcognate codons and programmed mitoribosome collision sites across the mitochondrial transcriptome, respectively. Our work provides a useful resource for delineating protein synthesis within this indispensable organelle.

Introduction

In eukaryotic cells, mitochondrial symbiogenesis provides another protein synthesis system in the organelle [1], in addition to one in the cytosol [2,3]. Although the human mitochondrial genome possesses only 13 mRNAs, translation in the mitochondrial matrix is indispensable for cells since these mRNAs encode a subunit of oxidative phosphorylation (OXPHOS) that is essential for ATP synthesis [4]. The importance of mitochondrial translation integrity has been illustrated by the pathological outcome of its dysregulation [5–7].

A variety of techniques have been developed to investigate translation in the organelle [8]. Among them, mitochondria-optimized ribosome profiling (or Ribo-Seq), which is based on deep sequencing of ribosome-protected RNA fragments remaining after RNase digestion [9], has been a powerful tool (MitoRibo-Seq) [10–16]. However, technical challenges have prevented the expansion of MitoRibo-Seq into a simple, low-input-tailored, and sample number-scalable tool. Thus, there is still much room for improvement in MitoRibo-Seq.

Related to the issues described above, our knowledge of mitochondrial translation kinetics in cells has been limited. This is in stark contrast to the case for cytosolic translation, where kinetic information has been generated by *in vivo* single-molecule imaging [17–23] and cytosolic ribosome profiling [24–26].

To extend our understanding of mitochondrial translation, we developed MitoIP-Thor-Ribo-Seq. Mitochondrial immunoprecipitation (MitoIP) with an antibody targeting the outer membrane protein TOM22 allows rapid purification of mitochondrial ribosomes with parallel handling of multiple samples simultaneously. Moreover, the implementation of an RNA-dependent RNA amplification technique [27] has enabled library preparation

from low-input materials after MitoIP. By combining a retapamulin-mediated mitochondrial ribosome (mitoribosome) run-off assay and an absolute calibration technique [26], we measured key kinetic and stoichiometric parameters of *in organello* translation, including translation initiation and elongation rates. Extremely slow elongation and recycling events were further unveiled by sequencing footprints generated by collided mitochondrial disomes (mito-disomes). Moreover, retapamulin-assisted MitoIP-Thor-Ribo-Seq revealed subcognate cryptic translation initiation sites in the mitochondrial transcriptome. We further employed our method to study the role of mitochondrial tRNA (mt-tRNA) modifications at the 34th and 37th positions. This method provides a versatile and high-resolution tool to monitor *in organello* protein synthesis, and our results serve as valuable data resource for future studies.

Results

Development of MitoIP-Thor-Ribo-Seq

The sucrose density gradient with ultracentrifugation has been applied to enrich mitoribosomes and their footprints and deplete cytosolic ribosome (cytoribosome) footprints in order to survey mitochondrial translation by Ribo-Seq [8,10–16]. A drawback of this strategy is in its limitation in handling many samples (*i.e.*, the maximum number of samples is limited to the 6 tubes that the ultracentrifuge rotor holds) as well as its time-consuming nature (~1 d). To overcome this issue, we employed mitochondrial immunoprecipitation (MitoIP) with an anti-TOM22 antibody and then treated the mitoribosome-enriched material with RNase to generate the footprints (Figure 1A). The MitoIP approach effectively concentrated mitoribosomes (55S, 39S, and 28S) from HEK293 cells, as detected in the sucrose density gradient, whereas the signal of mitochondrial ribosome complexes could not be detected in total cell lysates due to the large excess of cytosolic ribosomes (Figure 1B).

We systematically optimized the library construction procedures for mitoribosome footprints (or MitoIP-Ribo-Seq) using HEK293 cell lysate. Since ribosome isolation after RNase treatment was crucial to enrich footprints and exclude the nonfootprint RNA fragments, we tested the sucrose cushion with ultracentrifugation and size-exclusion gel-filtration spin column [28] and found that the former was more effective (Figure S1A). Given that RNase selection and the treatment condition define the quality of ribosome profiling data [29–32], we optimized the application in terms of RNase type (RNase I or the mixture of RNase A and RNase T1) and concentration (low and high) (Figure S1B). Moreover, we tested ribosome inhibitors in MitoIP-Ribo-Seq (Figure S1B and S1C), since compounds that halt ribosome movement along mRNA are also pivotal

factors in these experiments [33–39]. Notably, we omitted the drug treatment of the cell culture and instead added the drugs to the buffer for cell lysis (postlysis treatment) [40] to avoid potential artifacts introduced by pretreatment in cell culture [35–37,39]. In addition, we harnessed the recently developed Ribo-FilterOut technique to reduce rRNA contamination and increase the sequencing space (Figure S1D) [26]. To evaluate the quality of the ribosome profiling data, we defined the periodicity score (Figure S1E and S1F) to evaluate the 3-nt periodicity, which is a hallmark of ribosome profiling data with high codon resolution.

Ultimately, we found that MitoIP-Ribo-Seq with chloramphenicol-mediated mitoribosome elongation block and the high concentration of RNase I showed the highest performance (Figure 1C), providing mitoribosome footprints that peaked at 31-32 nt (Figure S1B). Compared to standard Ribo-Seq, optimized MitoIP-Ribo-Seq provided a significant enrichment of mitoribosome footprints along ORFs (Figure 1D) with fine triplet periodicity (Figure 1E).

The mitoribosome footprint in our data sets reflected the characteristic features of mitochondrial mRNAs. As 8 of 13 mRNAs do not have a 5′ UTR [41], 55S mitoribosomes assembled on the start codons at the very 5′ ends of mRNAs should not have the RNA region to be protected by the mitoribosomes [16]. Consistent with this scenario, we observed shorter 20-nt footprints at the 5′ ends of mRNAs without 5′ UTRs (Figures 1F, S1G, and S1H). We found that the footprints at the start codons with longer 5′ UTRs were extended; for example, we observed 23-nt footprints for *MT-CO1* mRNA, which has a 3-nt 5′ UTR (Figure 1G), and 31-nt and 32-nt footprints for *MT-ATP6* (Figures 1H) and *MT-ND4* (Figure S1I), which have long 5′ UTRs.

Seven of 13 mRNAs require poly(A) tailing to generate a complete stop codon sequence (UAA) [41]. Our MitoIP-Ribo-Seq detected footprints on the poly(A)-generated stop codons (Figures 1I and S1J), suggesting that poly(A) tailing is highly efficient and that mitoribosomes translate mRNAs after polyadenylation predominantly.

Given the footprint length and start codon locations that should be in the P site of mitoribosomes (Figures 1F-H and S1G-I), the P-site position in footprints was determined to be 12 nt downstream from the 5′ ends (Figure 1J). Consistently, we observed the 5′ ends of footprints 15 nt upstream of the stop codons, which are positioned at the A site (Figures 1I and S1J). Taking the 3-nt periodicity (Figure 1E) into account, we concluded that our MitoIP-Ribo-Seq can assess mitoribosome locations at single-codon resolution.

Due to the process of mitochondria isolation, only a small amount of material is ultimately acquired, hampering robust library construction. Thus, we implemented the T7 High-resolution Original RNA (Thor)-Ribo-Seq approach, which is based on RNA-dependent RNA amplification [27]. The application of this technique did not influence the codonwise measurement of ribosome occupancy (Figure S1K). Therefore, we harnessed MitoIP-Thor-Ribo-Seq for downstream analysis. We note that although chloramphenicol used in our method has been proposed to cause context-selective inhibition of elongation (preference for Ala/Ser and disfavor for Gly) at the penultimate amino acid (or E site) in bacteria [42–46], our mitochondrial data did not show such a bias (Figure S1K).

Ultimately, compared to published conventional MitoRibo-Seq [10,11,13–16], our MitoIP-Thor-Ribo-Seq provided comparable or even superior results in mitoribosome footprint recovery (Figure 1K). Notably, the convenience of mitochondria isolation for multiple samples in parallel and the low-input-tailored library construction method allowed us to investigate mitochondrial translation in more than 60 samples in this study.

Kinetics of mitochondrial translation

During our survey of ribosome inhibitors for mitochondrial translation (Figure S1C), we noticed that retapamulin, a compound that traps bacterial ribosomes at the start codon but not actively elongating ribosomes [47], effectively blocked mitochondrial translation. This led us to perform a mitoribosome run-off assay to measure the mitochondrial translation elongation rate (Figure 2A) — pulse treatment with retapamulin to inhibit translation initiation, subsequent chase of preloaded mitoribosomes over time, and elongation arrest with chloramphenicol. This analysis should generate mitoribosome-free regions downstream of start codons (Figures 2A and S1L). Indeed, we observed the chase-time-dependent extension of the region (Figure 2B). Regression fitting revealed a global mitoribosome elongation rate of 0.42 codon/s (Figure 2C).

Our recent method for calibrating Ribo-Seq data (Ribo-Calibration) converts ribosome footprint counts to absolute numbers of ribosomes [26]. This analysis estimated differential mitoribosome numbers on transcripts (Figure 2D), while the number was generally low; on average, ~2 mitoribosomes were loaded on each mRNA. Some of the mRNAs were occupied by fewer than 1 mitoribosome, suggesting a pool of mitoribosome-free mRNAs. The sparseness was exemplified by the long distances between mitoribosomes (672 nt on average) (Figure S1M). Considering the mitoribosome numbers per transcript, the translation elongation rate calculated above, and ORF length, the translation initiation rate was determined to be 533 s/event (Figure 2E) (see Materials and Methods for details).

We further measured mRNA half-lives by 5′-bromo-uridine immunoprecipitation chase–deep sequencing (BRIC-Seq) [26,48,49] and found a range of mRNA half-lives similar

to those previously reported [50] (Figure 2F). This measurement allowed us to calculate the lifetime translation cycles before transcript decay; we determined that mitochondrial mRNAs were used for protein synthesis 26 times on average (Figure 2G).

Thus, our analysis revealed the stoichiometric and kinetic parameters of *in organello* translation (Figure 2H).

Widespread cryptic translation initiation sites

Given that retapamulin-mediated mitoribosome arrest at the start codon, we reasoned that long-duration incubation with this compound could be harnessed for translation initiation site surveys similar to those conducted for bacterial translation (with retapamulin) [47] and cytosolic translation in eukaryotes (with harringtonine or lactimidomycin) [25,51,52]. As expected, MitoIP-Thor-Ribo-Seq with retapamulin treatment identified sharp read peaks at all the annotated translation initiation sites both at the 5′ ends of mRNAs (Figures 3A-B, 3F-G, and S2C-I) and in the middle of transcripts in polycistronic *MT-ATP8*/*MT-ATP6* (Figure 3A) and *MT-ND4L*/*MT-ND4* mRNAs (Figure 3B). Accordingly, the short footprints that reflect mitoribosomes at the start codons of leaderless mRNAs (Figures 1F-G and S1G-H) were enriched by retapamulin treatment (Figure 3C).

Intriguingly, we also detected the accumulation of mitoribosome footprints at diverse positions in the mitochondrial transcriptome. Thus, we systematically surveyed the cryptic translation initiation sites using retapamulin-treated data. Considering annotated translation initiation sites as true positives, a receiver operating characteristic (ROC) curve defined the threshold of the unannotated translation initiation sites at 99% specificity (1% false positive rate) (Figure S2A-B) and identified 31 unannotated positions (Figure 3D-E). These cryptic translation initiation sites were often AUG or

AUA codons (Figure 3D), as found in annotated start codons or their subcognate sequences (22 out of 31) (Figures 3A-B, 3F-G, and S2C-I). A subset of in-frame initiation sites may generate N-terminal truncated proteins (Figure 3E). This set of newly identified translation initiation sites included a recently reported short ORF in the 3′ UTR of *MT-ND5* [*MT-ND5* downstream ORF (*MT-ND5-dORF*)] [16] (Figure 3F).

These data showed the unexpected complexity of start codon recognition in mitochondrial protein synthesis.

f^5C34 facilitates mitoribosome traversal of AUA codons

Harnessing the MitoIP-Thor-Ribo-Seq approach, we assessed the importance of tRNA modifications at position 34 (Figure S3A). We started the investigation of the effect of 5-formylcytidine (f^5C) on mt-tRNA^{Met} [53–56]. This modification, which is unique to mt-tRNA, is catalyzed in 3 steps by 2 enzymes (Figure 4A): cytidine (C) conversion to 5-methylcytidine (m^5C) (methylation) by NSUN3, followed by and m^5C conversion to 5-hydroxymethylcytidine (hm^5C) (hydroxylation) and hm^5C conversion to f^5C (oxidation) by ALKBH1 [53–56]. Although this modification has been suggested to be essential for AUA recognition by *in vitro* systems [57,58], its impact in cells remains elusive.

Here, we applied MitoIP-Thor-Ribo-Seq to *NSUN3* knockout (KO) cells [53] (Figures 4B-G and S3B-C). We explored the ribosome occupancy change on each codon induced by depletion of the gene. Consistent with the proposed functions of the modifications in decoding, we found a prominent accumulation of mitoribosome footprints on the AUA codon at the A site by *NSUN3* deficiency (Figure 4B). In stark contrast, the alteration of mitoribosome occupancy at the AUG codon was limited (Figure

4B). These data highlighted the significance of f^5C34 on mt-$tRNA^{Met}$; unmodified tRNAs C34 could not efficiently decode AUA in the A site.

Moreover, our data also indicated the role of f^5C34 in peptidyl transfer or mitoribosome translocation. We noticed that mitoribosomes were stalled when AUA was present at the P site in the mutant cells (Figure S3C). The change in mitoribosome occupancy along codon positions revealed the comparable effects of A-site and P-site AUA on mitoribosome slowdown (Figure 4C). The combination of AUA-AUA dicodons in the P and A sites led to further enhancements of overall mitoribosome stalling (Figure 4D). This phenotype was exemplified by remarkable mitoribosome footprint accumulation in an AUA-AUA dicodon in *MT-ND5* (Figure 4E).

In addition to the strong pinpoint effect on specific codons, the loss of f^5C34 modification may also alter the broad distribution of mitoribosomes along ORFs. We calculated polarity scores [59], which reflect the positional bias of footprints in ORFs (Figure S3D), and found that the distributions of mitoribosomes were shifted to 5′ areas in several mRNAs (Figure 4F). *MT-CO1*, which has a cluster of AUA codons from positions 50-100, provided such an example (Figure 4G).

To further extend our approach from cell culture to *in vivo* tissue, we employed the hearts from *Nsun*3 KO mice [60] (Figure S3E). The mitoribosome footprints from the mouse tissue also showed shorter mitoribosome footprints at start codons on mRNAs with absent or short 5′ UTR (Figure S3F-G). Our mouse heart data recapitulated the ribosome stalling at AUA-AUA dicodons, although the effect was less pronounced than that in cell culture (Figure 4H). We observed that the mitoribosome footprint distribution was biased toward the 5′ ends of transcripts possessing AUA clusters at the early ORF, such as *MT-CO1* and *MT-ND5* (Figures 4I and S3H-I). These data indicated the functional

conservation of f^5C34 in mammals and demonstrated the potency of our approach for *in vivo* study.

In addition to participating in elongation, mt-tRNA^{Met} should be used as the initiator tRNA [1,61]. To monitor the effect of modifications on translation initiation, we conducted standard Ribo-Seq (without MitoIP) and RNA-Seq to measure translation efficiency (*i.e.*, ribosome footprints normalized by RNA abundance) and found that mRNAs beginning with AUA and AUG did not show a consistent trend in translation efficiency change (Figures 4J). In contrast, AUU-initiated *MT-ND2* mRNA was activated in *NSUN3* KO cells. Thus, f^5C34 may function in translation initiation in an mRNA-dependent manner.

Influence of τm^{5}U34 for UUG, UGG, and AAG codons

Another mt-tRNA-specific decoration is taurine modification. This modification has been found in 5 mt-tRNAs: mt-tRNA$^{Leu\ (UUR)}$, mt-tRNA^{Trp}, mt-tRNA^{Lys}, mt-tRNA^{Gln}, and mt-tRNA^{Glu} that decode NNR codons (where R represents A or G). The MTO1-GTPBP3 complex catalyzes τm^{5}U using taurine and 5,10-methylenetetrahydrofolate (CH_2-THF) [13,62–65] (Figure 5A). Among these 5 tRNAs, U34 in mt-tRNA^{Lys}, mt-tRNA^{Gln}, and mt-tRNA^{Glu} is additionally modified to s^2U by MTU1 and is ultimately converted to τm^{5}s^{2}U34 (Figure 5A) [63,66–68]. The τm^5 and s^2 modifications are mutually independent [63].

MitoIP-Thor-Ribo-Seq with *GTPBP3* KO HEK293 cells [64] showed that the impact of τm^{5}U34 modification varies across codons decoded by the five mt-tRNAs (Figures 5B-J and S4A-B). First, τm^{5}U34 did not affect ribosome traversal on codons ending in A (UUA, UGA, AAA, CAA, and GAA) (Figure 5B-F), as taurine modification-free tRNA (U or s^{2}U) could base-pair with these codons. Second, among the G-ending

codons, UUG, UGG, and AAG led to mitoribosome stalling due to GTPBP3 depletion, whereas CAG and GAG showed limited effects (Figure 5B-F). The weak effect on GAG Glu codon may be associated with the low τm^5 modification rate on mt-tRNA^{Glu} at the basal level [64]. Third, both the A-site and P-site locations of the UUG, UGG, and AAG codons resulted in a mitoribosome slowdown (Figure 5B-D). UUG codons (located at the A site) in *MT-ND2* exemplified the mitoribosome stalling induced by *GTPBP3* KO (Figure 5G).

Overall mitoribosome distributions along the transcripts were also biased by *GTPBP3* KO (Figure 5H). *MT-ND6*, in which the mitoribosome footprint distribution was most disrupted, showed mitoribosome arrest at an AAG codon (P-site position) and concomitantly reduced mitoribosome flux downstream (Figure 5I).

During the data analysis, we noted the mitoribosome occupancy change beyond the codons that were recognized by the τm^5-modified mt-tRNA. We detected greater mitoribosome occupancy at CAU His codons (Figure 5J). This implied that τm^5-hypomodified mt-tRNA^{Gln}, which typically decodes the CAG and CAA codons, may compete with mt-tRNA^{His} for the CAU codon. Considering that a substantial fraction of mt-tRNA^{Gln} was not fully $\tau m^5 s^2$-modified at basal level and only possessed τm^5 [69], GTPBP3 depletion may increase the unmodified U34 in mt-tRNA^{Gln}. Since mt-tRNA with U34 could recognize all the four bases (U, A, G, and C) at the wobble position (*i.e.*, 4-way wobbling) [61], the hypomodified mt-tRNA^{Gln} may have more high frequency to misread the nearcognate CAU codon. Thus, ultimately, the CAU codon may require a longer time to be decoded by mt-tRNA^{His}.

MELAS-causing mt-tRNA mutation leads to mitoribosome queuing

τm^{5}U deficiency has been implicated in diseases such as mitochondrial myopathy, encephalopathy, lactic acidosis, and stroke-like episodes (MELAS). The most frequent mutation associated with MELAS is A3243G in the mitochondrial genome; this site corresponds to the 14th position of mt-tRNA$^{Leu\ (UUR)}$ [70–72] (Figure 6A). Destabilization of the conformation by the mutation [73,74] may cause the tRNA to become a poor substrate of the MTO1-GTPBP3 complex and thus reduce its τm^{5}U modification rate [64,75–77].

We explored the translational dynamics in the myoblasts of a MELAS patient with A3243G [78] with MitoIP-Thor-Ribo-Seq (Figures 6B-G and S5A-B). Consistent with earlier biochemical work [79], we observed the accumulation of mitoribosomes at UUG codons (Figure 6B), as found in *GTPBP3* KO cells (Figure 5B). Again, the footprint accumulation at both P and A sites suggested a function for τm^{5}U in decoding and translocation. This pausing was represented by a UUG codon in *MT-ND2* (Figure 6C). In stark contrast, no alteration of reads on UUA codons was observed (Figure 6B).

Strikingly, we observed mitoribosome queuing in MELAS patient cells. A metagene plot around UUG codons revealed 2 upstream peaks at 11-12 codon intervals (Figure 6D), which is the size of a mitoribosome (Figure 1J), indicating the formation of collided mito-disomes and mito-trisomes. In contrast, the mitoribosome distribution around UUA codons was not affected (Figure S5B). These data clearly indicated that severe mitoribosome stalling occurs in MELAS patients.

We also noted a bias in footprint distribution toward the 5′ ends of the ORFs in *MT-ND6* and *MT-ND5* (Figure 6E-G). These data explain the remarkable reduction in the synthesis rate of these proteins reported in previous studies [78]. *MT-ND6* is the most UUG-rich mRNA, which has been proposed to explain the susceptibility of MT-ND6 protein

synthesis to disruption in MELAS [79]. Our mitoribosome distribution findings suggest another cause for the high sensitivity of *MT-ND6*.

s^2U decorations for efficient GAG translation and the suppression of cryptic GAC misreading

Since mt-tRNA^{Lys}, mt-tRNA^{Gln}, and mt-tRNA^{Glu} have s^2 modifications at U34 [63,66–68] (Figure 5A), we also investigated the role of this modification in mitochondrial translation using *MTU1* KO cells, which were generated by CRISPR-Cas9-mediated genome editing (Figures 7A-E and S6A-D). The loss of MTU1 protein and s^2 modification in mt-tRNA were validated by Western blotting and mass spectrometry, respectively (Figure S6A-B). Among the three mt-tRNAs possessing s^2U34, the GAG codon showed the strongest mitoribosome pauses (Figure 7A-C), suggesting dysfunction of mt-tRNA^{Glu}. In addition, we also detected that the subcognate GAC Asp codon of this tRNA accumulated in mitoribosomes (Figure 7D), as if s^2-hypomodified mt-tRNA^{Glu} with unmodified U34 misread nearcognate GAC codons. *MT-CO1* provided an example of mitoribosome stalling on GAG and GAC codons (Figure 7E). Given that similar misreading and resultant mitoribosome slowdown were not found in τm^5-deficient cells (Figure S4B), the fidelity maintenance function was assigned to s^2 but not $\tau m^5 s^2$. These data provide another example of codon misreading induced by tRNA modification deficiency.

Mitoribosome traversal is modulated by queuosine modification

Queuosine (Q) provides another regulatory layer of protein synthesis [69,80]. This modification is found in both cytosolic and mitochondrial tRNAs and is mediated by the QTRT1-QTRT2 complex, a guanine transglycosylase [81]. In mitochondria, G34-to-Q34

modification was found in mt-tRNA^{Asn} (for AAU and AAC codons), mt-tRNA^{His} (for CAU and CAC codons), mt-tRNA^{Asp} (for GAU and GAC codons), and mt-tRNA^{Tyr} (for UAU and UAC codons) [69] (Figure 8A). Our conventional Ribo-Seq showed mitoribosome stalling at the UAU Tyr codon upon *QTRT2* KO [69]; here, we revisited the effects of Q modification in detail with the new improved method.

Our highly sensitive detection by MitoIP-Thor-Ribo-Seq unveiled further fine tuning of mitochondrial elongation by Q (Figures 8B-C and S7A-D). Among the U-ending codons on the A site, MitoIP-Thor-Ribo-Seq revealed mitoribosome accumulation at UAU Tyr codons in both *QTRT1* KO and *QTRT2* KO cells, as reported previously [69] (Figure 8B). In addition, for codons ending in C, QTRT1 and QTRT2 depletion reduced the mitoribosome footprints on AAC at the A site (Figure 8C), suggesting that Q could retard mitoribosome traversal of these codons. Thus, Q modification can impede or promote mitoribosome traversal, depending on the codon.

t^{6}A primarily impacts Lys codon elongation

In addition to modification in the 34th position, we studied a modification at the 37th position, 3′ adjacent to the anticodon (Figure S3A). Generally, the modification of this position was thought to contribute to accurate codon recognition and the prevention of frameshift errors [82,83]. We investigated the *N*^{6}-threonylcarbamoyladenosine (t^{6}A) modification at this position [69]. This modification, catalyzed by OSGEPL1 [84], is found in mt-tRNAs responsible for ANN codons: mt-tRNA^{Lys}, mt-tRNA^{Asn}, mt-tRNA^{Thr}, mt-tRNA^{Ile}, and mt-tRNA$^{Ser\,(AGY)}$ (where Y represents U or C) (Figure 9A).

MitoIP-Thor-Ribo-Seq analysis of *OSGEPL1* KO cells [84] (Figures 9B-J and S8A-B) showed that among all the codons recognized by t^{6}A37-modified mt-tRNA, OSGEPL1

deficiency led to mitoribosome stalling, predominantly at AAG codons and modestly at AAA codons (Figure 9B-G). At both the A site and P site positions of AAG/AAA codons, mitoribosome traversal was slowed by t^6A37 deficiency. An AAG codon in *MT-CO1* provided a remarkable example of mitoribosome stalling (Figure 9H).

The mitoribosome footprint distribution was biased toward the 5′ end in *MT-ND6* (Figure 9I). AAG at the 21st codon (at the P-site position) induced mitoribosome stalling and a subsequent reduction in mitoribosome traversal downstream (Figure 9J). Strikingly, the same codon position was similarly sensitive to the loss of τm^5U34 modification (Figure 5I).

Moreover, we noticed that CCU Pro codons showed higher mitoribosome occupancy upon OSGEPL1 deletion (Figure 9K). This may be caused by a misreading of CCU codons by mt-$tRNA^{Thr}$, which typically decodes ACU codons.

Overall, MitoIP-Thor-Ribo-Seq allowed us to evaluate the significance of all the modifications at the 34th position and a well-conserved modification at the 37th position in mt-RNA and to reveal the unexpected specificity of those modifications for codon and fidelity maintenance function (Figure S9).

Investigation of mitoribosome collision

Along with the mt-tRNA modifications that facilitate smooth elongation, the programmed slowdown of mitoribosome traversal may benefit protein synthesis. Given the importance of cotranslational insertion of the transmembrane domain [85–91] and cotranslational complex assembly [92], mitoribosome stalling may provide time for nascent peptides to target the membrane and interact with assembly factors.

To survey ribosome stall sites at high resolution, longer ribosome footprints generated by collided cytoribosomes have been analyzed (disome profiling) [93–103]. Here, we applied the same strategy to mitoribosomes, focusing on 50- to 80-nt long RNA fragments generated by RNase treatment of isolated mitochondrial fractions (Figure 10A), and found footprints of the expected size (Figure S10A) (MitoIP-Thor-Disome-Seq).

To precisely assess the position of leading, stalled mitoribosomes in the mito-disome footprints, we harnessed mitoribosome stalling on AUA-AUA dicodons (codon position 312-313, counting the start codon as position 0) on *MT-ND5* by *NSUN3* KO (Figure 4E). In naïve HEK293T cells, mito-disome footprints were quite sparse in this region (Figure 10B top). However, NSUN3 depletion dramatically increased the number of reads around the AUA-AUA dicodon (Figure 10B bottom). Considering the distance between the 5′ end of the read and the AUA-AUA dicodon, the A-site offset was determined to be 54 nt for mito-disome footprints (Figure 10C). This A-site assignment on reads enabled us to assess the position of stalled mitoribosomes at codon resolution. In addition to *MT-ND5* (Figure S10B), we found a striking peak of mito-disome footprints on AUA-AUA dicodons on *MT-ND1* (Figure S10C-D). Since the mito-disome fraction did not include normally elongating mitoribosomes, MitoIP-Thor-Disome-Seq allowed further sensitive detection of mitoribosome pause sites in *NSUN3* KO (Figure S10E-F).

MitoIP-Thor-Disome-Seq identified mitoribosome collision events that occurred naturally, even in the absence of mt-tRNA modification defects. We found differential occurrence of mito-disome and mito-monosome footprints across mRNAs (Figure 10D). Among the mito-disome-rich transcripts, we observed a sharp accumulation of mito-disome footprints at specific codons (Figures 10E-G and S10G-H). Considering that the mitoribosome exit tunnel accommodates amino acids 30-40 of the nascent peptide [91], the

mito-disome pause sites were well assigned to the position where the completed transmembrane domain (TMD) is exposed to solvent. For example, position 446 on *MT-CO1* allowed the synthesis of TMD10, with the C-terminal end facing the matrix (Figure 10E and 10H). A similar topology between TMD synthesis and mito-disome pause sites was found in *MT-CO1* TMD12, *MT-CO3* TMD6, *MT-CYB* TMD2, *MT-ND6* TMD1, and *MT-ATP8* TMD1 (Figures 10E-H and S10G-I). We note that due to the overlapping ORFs of *MT-ATP8* and *MT-ATP6* in the bicistronic transcript, we could not clearly distinguish whether the leading mitoribosome in the mito-disome (codon 65 in *MT-ATP8* position) (Figure S10H) was on *MT-ATP8* or *MT-ATP6*, although the trailing mitoribosome should be translated with *MT-ATP8* (Figures S10I).

On *MT-CO1,* in which mitoribosome collision frequently occurred, we found significant mito-disomes on the noncanonical AGA stop codon [41] (position 513), suggesting inefficient termination/recycling of this noncanonical stop codon (Figure 10E). Furthermore, mitoribosomes may form a long queue, as indicated by monitoring mito-disomes ~10 codons upstream (position 502) and ~20 codons upstream (position 491) (Figure 10E). Thus, the noncanonical AGA stop codon serves as the source of mitoribosome queuing (Figure 10I left).

In addition to the ORF, we found mito-disome formation on the 3′ UTR of *MT-CO1* (position 523) (Figure 10E). The leading paused mitoribosome was located 10 codons downstream of the stop codon, the size of a single mitoribosome, whereas the trailing mitoribosome was on the ORF. As the unrecycled cytoribosome could be "pushed" by translating ribosomes and form disomes until the trailing ribosomes reach the stop codons [97,98], this mito-disome may be produced by the same scenario (Figure 10I right).

Altogether, MitoIP-Thor-Disome-Seq offers a means to monitor elongation slowing, termination, and recycling events in mitochondrial protein synthesis.

Discussion

The improved mitochondrial ribosome profiling methods developed here illustrated an *in organello* translation landscape that was not accessible with preexisting approaches. We found that mitochondrial translation kinetics were strikingly different from those of cytosolic translation (Figure 2): the elongation rate was ~10 times slower (0.42 codon/s in mitochondria vs. 4-5 codon/s in the cytoplasm) [24–26,104]; compared to the elongation rate, the initiation rate was generally slow and rate-limiting in both translation systems but more extreme in mitochondria (533 s/event in mitochondria vs. ~22 s/event in the cytoplasm) [26]. These inefficiencies may be compensated for by the high expression of mitochondrial mRNAs (Figure S10J). As a consequence, mitochondrial mRNAs were translated only a limited number of times (~26 times in mitochondria vs. ~1800 times in the cytoplasm). We note that the mitochondrial translation initiation speed could vary among cell types, as differences in the global mitochondrial protein synthesis rate have been detected [105].

The function of τm^5U34 in mitochondrial translation suggested by this study was largely consistent with an earlier report that applied conventional MitoRibo-Seq in *MTO1* KO cells and A3243G MELAS patient cells [13]. Our improved methods further extended our understanding of τm^5U34's role in mitochondrial translation fidelity (*i.e.*, the suppression of competition of mt-tRNA^{Gln} with mt-tRNA^{Asp} for CAU Asp codon). Moreover, our data also revealed long queues of mitoribosomes upstream of UUG codons in MELAS patient cells. These data highlighted the utility of MitoIP-Thor-Ribo-Seq in detecting translational events that could not be captured by earlier methods.

Our data unveiled the functional similarities and differences of specific modifications between mitochondrial and cytosolic tRNAs. Q34 is also found in cytosolic

tRNAs (ct-tRNA) decoding the same set of codons (*i.e.*, ct-tRNA^{Asn}, ct-tRNA^{His}, ct-tRNA^{Asp}, and ct-tRNA^{Tyr}) [106,107]. Standard Ribo-Seq with cells cultured in Q-depleted media showed slow decoding of all the U-ending codons (such as AAU, CAU, GAU, and UAU) [80] but more profoundly than that we found for mitochondria (Figures 8 and S7). This suggested that the two translational systems rely on the Q modification to different extents.

s^2U34 was found in the same tRNA species in the cytosol and mitochondria (*i.e.*, ct-tRNA^{Lys}, ct-tRNA^{Gln}, and ct-tRNA^{Glu}). These base positions are simultaneously modified with 5-metoxycarbonylmethyl (mcm^5) and ultimately form mcm^5s^2U34 [61]. Thus, mcm^5 in cytosolic tRNA could be a counterpart of τm^5 in the mitochondria. In contrast, the loss of mcm^5 and s^2 in cytosolic tRNA does not impact the wobble pairing codons (G-ending) of AAG, CAG, and GAG [108–110], which are critically impacted by mitochondrial τm^5 and s^2 (Figures 5 and 7). Rather, those modifications facilitate the decoding of Watson-Crick pairing (A-ending) codons of AAA, CAA, and GAA [108–110]. Nonetheless, mcm^5 in ct-tRNA^{Gln} and τm^5 in mt-tRNA^{Gln} shared the ability to suppress miscoding of subcognate CAU codons (Figure 5J) [109]. Our study illuminated the distinction in the functionality of similar (mcm^5 vs. τm^5) and identical (s^2) modifications at U34 positions in the two translation systems.

The role of t^6A37 modification in cytosolic tRNAs, including the same five ct-tRNAs as in mitochondrial counterparts, ct-tRNA^{Met}, and ct-tRNA$^{Arg\ (AGR)}$ (where R represents A or G), has been investigated in yeast Ribo-Seq [110,111]. The data indicated that t^6A37 has pleiotropic effects: it may increase the elongation rate of U-ending codons (ANU), whereas it has the opposite effect in C-ending codons (ANC). Our data showed more limited effects on translation; AAG and AAA codon decoding were only facilitated

by t^6A37 (Figure 9). Another important activity of t^6A37 in cytosolic tRNAs is fidelity maintenance by suppressing leaky scanning, stop codon readthrough, and frameshifting [112]. However, the molecular basis of this function is attributed to prevention of the competition of t^6A37-modified elongator $tRNA^{Met}$ with nonmodified initiator $tRNA^{Met}$ [112]. On the other hand, in mitochondria, the same mt-$tRNA^{Met}$ serves both translation initiation and elongation functions and is not modified by t^6A37 [69]. Thus, mitochondrial t^6A37 should not have such a role. Indeed, our data did not show evidence of stop codon readthrough (Figure S8B).

The mechanism of translation strat for the cryptic translation initiation sites remained elusive. Although 55S, not 28S, could be directly loaded onto the initiation codons at the 5′ termini of mRNAs [113], the internal initiation codons should be recognized with a distinct mechanism. As proposed for polycistronic transcripts of *MT-ATP8*/*MT-ATP6* and *MT-ND4L*/*MT-ND4* [114], the terminated mitoribosome for a main ORF may be reused at cryptic translation initiation sites. This process may be facilitated by mtIF3 [113].

Through the development of MitoIP-Thor-Disome-Seq, we unveiled mitoribosome arrest sites at single-codon resolution. An earlier work biochemically predicted mitoribosome pauses in *MT-CO1* mRNA at the ~212 and ~280 codon positions, which engage a Complex IV assembly intermediate termed MITRAC [92]. However, the corresponding sites were not identified in our mito-disome profiling or even mito-monosome profiling (Figure 10E). At present, we cannot explain this discrepancy. Future studies, such as the isolation of MITRAC and associated mitoribosome and subsequent mito-monosome/disome profiling, will uncover the pause sites accompanied by complex assembly.

Despite the low elongation rate and the sparse mitoribosome presence on mRNAs, we observed the mitoribosome collision at specific codon positions, suggesting that these contexts cause significantly slower mitoribosome movement. It may be expected that a high mitoribosome loading rate may increase the probability of mitoribosome collision. However, counterintuitively, we observed the opposite trend; mito-disome-rich mRNAs such as *MT-ND6*, *MT-CO3*, and *MT-CO1* (Figure 10D) showed slow initiation rates (Figure 2F). This may suggest the opposite mechanism; the mito-disome represses translation initiation. Indeed, cytosolic ribosome collision induces ribosome-associated quality control (RQC) that ultimately represses the loading of further ribosomes on mRNA recruiting initiation repressor (4EHP) [115]. A similar feedback loop may exist in mitochondria.

Acknowledgments

We thank all the members of the Iwasaki laboratory for constructive discussion and technical assistance. We also thank Dr. Nono Takeuchi-Tomita for fruitful comments on this work. S.I. was supported by the Ministry of Education, Culture, Sports, Science and Technology (MEXT) [Grant-in-Aid for Transformative Research Areas (B) "Parametric Translation", JP20H05784], the Japan Society for the Promotion of Science (JSPS) [Grant-in-Aid for Scientific Research (B), JP23H02415], the Japan Agency for Medical Research and Development (AMED) (AMED-CREST, JP23gm1410001), the Gushinkai Foundation, and RIKEN ("Biology of Intracellular Environments"). Y.S. was supported by JSPS [Grant-in-Aid for Early-Career Scientists, JP21K15023; Grant-in-Aid for Scientific Research (C), JP23K05648]; MEXT [Grant-in-Aid for Transformative Research Areas (A) "Multifaceted Proteins", JP21H05734, JP23H04268]; and RIKEN (Incentive Research Projects). T.W. was supported by The Graduate School of Frontier Sciences, The University of Tokyo (the Challenging New Area Doctoral Research Grant, C2205 and C2306)]; JSPS (Grant-in-Aid for JSPS Fellows, JP23KJ0444). A portion of the DNA libraries were sequenced at the Vincent J. Coates Genomics Sequencing Laboratory at QB3 Genomics, UC Berkeley, Berkeley, CA (RRID:SCR_022170), with support by the NIH S10 OD018174 Instrumentation Grant. Computations were supported by the supercomputer HOKUSAI SailingShip in RIKEN. We are grateful to the Support Unit for Bio-Material Analysis, RIKEN CBS Research Resources Division, for Sanger sequencing. T.W. was a recipient of fellowships from JSPS (DC2), JST SPRING (JPMJSP2108), and the ANRI. H.T. was a JSPS postdoctral fellow (PD).

Author contributions

Conceptualization, T.W. ,M.M., H.Y., and S.I.;

Methodology, T.W., M.M., H.Y., Kotaro T., H.T., Y.S., and S.I.;

Formal analysis, T.W., H.Y., Kotaro T., H.T., Y.S., and S.I.;

Investigation, T.W., M.M., H.Y., Kotaro T., H.T., and Y.S.;

Resources, H.T., Kazuhito T., T.C., A.N., Takeo S., F.Y.W., and Tsutomu S.;

Writing – Original Draft, T.W. and S.I.;

Writing – Review & Editing, T.W., M.M., H.Y., Kotaro T., H.T., Kazuhito T., T.C., A.N., Takeo S., F.Y.W., Y.S., Tsutomu S., and S.I.;

Visualization, T.W. and S.I.;

Supervision, F.Y.W., Kazuhito T., T.C., A.N., Takeo S., Y.S., Tsutomu S., and S.I.;

Project administration, S.I.;

Funding Acquisition, T.W., Y.S., and S.I.

Materials and Methods

Cell lines

NSUN3 KO, *GTPBP3* KO, *QTRT1* KO, *QTRT2* KO, and *OSGEPL1* KO HEK293 cells were generated previously [53,56,64,69,84]. Wild-type or A3243G-mutated myoblasts were previously derived from a muscle sample from a MELAS patient and clonally selected [77,78]. The cell lines above, along with naïve HEK293 cells [American Type Culture Collection (ATCC), CRL-1573] were cultured at 37°C with 5% CO_2 in the media described in Table S1. An e-Myco VALiD Mycoplasma PCR Detection Kit (iNtRON Biotechnology) was used to confirm that the culture was free of *Mycoplasma*.

Animals

Male wild-type mice and heart-specific *Nsun3* KO mice were acquired previously [60]. Mice were housed at 25°C with a 12-h:12-h light-dark cycle. The experiment was performed at 8 weeks old. After sacrifice, the cardiac muscles were dissected, immediately flash-frozen in liquid nitrogen, and stored at −80°C. All animal experiments were authorized and approved by the animal ethics committee of Kumamoto University (approval ID: A2021-012R3 and A2023-011).

Generation and validation of MTU1 KO cells

MTU1 KO HEK293 cells were generated using the CRISPR-Cas9 system. A guide RNA sequence was selected to target exon 1 of *MTU1* and cloned into the LentiCRISPR v2 (a gift from Feng Zhang, Addgene plasmid # 52961; http://n2t.net/addgene:52961; RRID:Addgene_52961) [116]. The targeting sequence is 5′-GCTGTCCACGCCGCCGGGACA-3′. Cells were infected with lentivirus carrying the

above gRNA and Cas9 gene and selected with puromycin for 3 d. Single colonies were selected using a cloning disc. Total cell lysates from candidate cell lines were subjected to Western blotting. Total RNA from each candidate cell line was digested to single nucleoside using nuclease P1 (Fujifilm Wako Pure Chemical Corporation) and bacterial alkaline phosphatase (TaKaRa), followed by mass spectrometry analysis, as previously described [67]. The MTU1-mediated mitochondrial tRNA τm^5s^2U (*m/z* 398.0686) modification was detected using a Q Exactive mass spectrometer (Thermo Fisher Scientific) in full mass scan and positive ion mode. ms^2i^6A (*m/z* 382.1543), a mitochondrial tRNA specific modification, was used as a control for mitochondrial RNA loading.

MitoIP-Ribo-Seq, MitoIP-Thor-Ribo-Seq, and MitoIP-Thor-Disome-Seq

Lysate preparation

Cells were cultured in 15-cm dishes, washed with ice-cold PBS, and lysed with 1200 µl of hypotonic buffer (10 mM HEPES-KOH pH 7.5, 10 mM KCl, 1.5 mM $MgCl_2$, 1 mM DTT, 100 µg/ml cycloheximide, and 100 µg/ml chloramphenicol). The lysate was incubated with anti-TOM22 antibody-conjugated beads from the Mitochondria Isolation Kit, Human (Miltenyi Biotec) for 60 min at 4°C. The subsequent wash and elution steps were performed with wash buffer (10 mM HEPES-KOH pH 7.5, 10 mM KCl, 15 mM $MgCl_2$, 1 mM DTT, 100 µg/ml cycloheximide, and 100 µg/ml chloramphenicol) according to the manufacturer's instructions. The eluted mitochondrial fraction was pelleted by centrifugation at 7,000 × g for 10 min at 4°C and resuspended in modified lysis buffer (20 mM Tris-HCl pH 7.5, 150 mM NaCl, 15 mM $MgCl_2$, 1 mM DTT, 1% Triton X-100, 100 µg/ml cycloheximide, 100 µg/ml chloramphenicol, and 2.5 U/ml

TURBO DNase). After clarification by centrifugation at 20,000 × g for 10 min at 4°C, the supernatant was subjected to library preparation.

For the mitoribosome run-off assay, HEK293 cells were pretreated with 100 μg/ml retapamulin for 30, 60, 90, 120 s, or 30 min and then incubated with 100 μg/ml chloramphenicol and 100 μg/ml cycloheximide to arrest translation elongation. Subsequently, cell lysis and mitochondrial purification were performed as described above, adding 100 μg/ml retapamulin to all the solutions.

Mouse cardiac muscle

Frozen myocardium was pulverized with 600 μl of liquid nitrogen-frozen hypotonic buffer using the Multi-beads Shocker (Yasui Kikai) at 3000 rpm for 30 sec for 2 cycles. The lysate was clarified by an EASYstrainer (Greiner Bio-One), and mitochondria isolation was conducted as described above.

Library preparation; MitoIP-Ribo-Seq

The lysate was incubated with 2 U of RNase I (LGC Biosearch Technologies, low), 10 U of RNase I (high), 0.12 U RNase A/T1 (Thermo Fisher Scientific, low), or 0.6 U RNase A/T1 (high) in a 50 μl reaction (scaled up by the modified lysis buffer) at 25°C for 45 min. Then, for Ribo-FilterOut [26], the mitoribosomes were pelleted by sucrose cushion and resuspended in EDTA lysis buffer [20 mM Tris-HCl pH 7.5, 150 mM NaCl, 15 mM $MgCl_2$, 1 mM DTT, 5 mM EDTA, 1% Triton X-100, and 20 U/ml SUPERase•In RNase inhibitor (Thermo Fisher Scientific)]. The solution was loaded onto an Amicon Ultra 0.5 ml Ultracel 100K centrifugal filter (Millipore) and centrifuged at 14,000 × *g* at 4°C for 10 min [26]. The RNA from the flowthrough was purified with TRIzol LS (Thermo Fisher

Scientific) and a Direct-zol RNA MicroPrep Kit (Zymo Research) and separated on a 15% UREA PAGE gel. Fragments ranging from 17 to 50 nucleotides (nt) were excised from the gel. Subsequent library generation was followed by an earlier report [28]: RNA fragments were dephosphorylated and ligated with linkers; rRNA depletion was conducted by the Ribo-Zero Gold rRNA Removal Kit (Human/Mouse/Rat) (Illumina, accompanied by TruSeq Stranded Total RNA Kit); cDNA was reverse-transcribed, circularized by ligation, and PCR-amplified. Sequencing of the DNA libraries was performed on a HiSeq 4000 in 50-bp single-read mode.

To test translation inhibitors, chloramphenicol in hypotonic buffer, wash buffer, and modified lysis buffer was replaced with capreomycin, blasticidin S, or tigecycline.

Size-exclusion gel-filtration spin column was conducted as described previously [28].

Library preparation; MitoIP-Thor-Ribo-Seq and MitoIP-Thor-Disome-Seq

Library preparation was conducted as described above with modifications. The lysate was incubated with 40 U of RNase I (LGC Biosearch Technologies) in a 50 µl reaction (brought up to volume with the modified lysis buffer) at 25°C for 45 min. Fragments ranging from 17 to 50 nt for monosomes and from 50 to 80 nt for disomes were collected. Then, libraries were prepared as previously reported [27]. From linker-ligated RNA fragments, rRNAs were depleted with Human Ribo-Seq riboPOOL (siTOOLs Biotech). Then, an oligonucleotide was hybridized to the T7 promoter region of the linker to generate the dsDNA T7 promoter. Complementary RNAs were transcribed by a T7-Scribe Standard RNA IVT kit (CELLSCRIPT). After ligation of the second linker, cDNA

was reverse-transcribed and PCR-amplified. DNA libraries were sequenced on HiSeq X Ten in 150-bp paired-end mode.

Standard Ribo-Seq and RNA-Seq

Lysate preparation

Approximately 1×10^7 cells in a 10-cm dish were lysed with 600 µl of lysis buffer (20 mM Tris-HCl pH 7.5, 150 mM NaCl, 5 mM $MgCl_2$, 1% Triton X-100, 1 mM DTT, 100 µg/ml cycloheximide, and 100 µg/ml chloramphenicol) and treated with 25 U/ml TURBO DNase (Thermo Fisher Scientific) [28]. Then, the lysate was clarified by centrifugation at 20,000 × g for 10 min at 4°C.

Library preparation

Ribo-Seq library preparation was performed according to a previously described protocol [26,28]. After RNase digestion and sucrose cushion ultracentrifugation, Ribo-FilterOut was conducted. Then, ribosome footprints ranging from 17-34 nt were gel-excised.

For RNA-Seq, total RNA was extracted from the same lysate used for Ribo-Seq with TRIzol LS (Thermo Fisher Scientific) and a Direct-zol RNA MicroPrep Kit (Zymo Research). Four hundred nanograms of total RNA was used with a SEQuoia Express Standard RNA Library Prep Kit (Bio-Rad).

For both library preparations, rRNA depletion was performed with the Ribo-Zero Gold rRNA Removal Kit (Human/Mouse/Rat) (Illumina, accompanied by TruSeq Stranded Total RNA Kit). Libraries were sequenced on a HiSeq X Ten in 150-bp paired-end mode.

Data analysis

Deep sequencing data processing was performed as described previously [117,118] with modifications. For the paired-end sequencing, fastp (version 0.21.0) [119] was used for base correction, and read 1 was processed for the downstream analysis. Read quality filtering and adapter sequence removal were conducted by fastp. All reads were aligned to noncoding RNAs (rRNAs, tRNAs, mt-rRNAs, mt-tRNAs, snRNAs, snoRNAs, and miRNAs), and the remaining reads were then mapped to the human or mouse nuclear genomes (human, hg38; mouse, mm10) and a custom database of mitochondrial transcript sequences using STAR (version 2.7.0a) [120]. For MitoIP-Thor-Ribo-Seq and MitoIP-Thor-Disome-Seq, duplicated reads were suppressed according to the unique molecular index (UMI) in the linkers using UMItools (version 1.1.2) [121].

Ribosomal A-site offsets for each footprint length were empirically estimated (Table S1). For the analysis of the first 5 codons, the dedicated A-site offsets were estimated separately considering the short or absent 5′ UTR in mitochondrial mRNAs (except for *MT-ATP6* and *MT-ND4*) (Table S1).

The relative entropy (Kullback–Leibler divergence) of H_j for read length j was defined as follows:

$$H_j = \left(-\sum_{i=-1}^{1} p_{random} log_2 p_{random}\right) - \left(-\sum_{i=-1}^{1} p_{ji} log_2 p_{ji}\right)$$

where p_{ji} is the fraction of mitoribosomes with footprint length j at frame i and p_{random} is 0.333. Then, the periodicity score (P) was defined as follows:

$$P = \sum_{j=12}^{40} H_j F_j$$

where F_j represents the fraction of mitoribosomes with footprint length j.

To calculate mitoribosome occupancy, the reads of each codon were normalized by the average reads per codon of the mitochondrial transcript. We omitted overlapping ORF regions in the bicistronic transcripts from the calculation (except where indicated in the figure panel legends).

The polarity score was defined as previously reported [59].

To calculate translation efficiency, a generalized linear model in the DESeq2 package [122] was used based on the relative enrichments of standard Ribo-Seq reads in ORFs over those in RNA-Seq. Reads assigned to the first and last 5 amino acids were excluded from this analysis.

For the mitoribosome run-off assay, smoothed metagene profiles were plotted from the mitochondrial transcripts, excluding *MT-ATP6* and *MT-ND4*. The mean read density from 100 to 200 codons was set to 1. The absolute mitoribosome numbers and half-life of the mitochondrial transcript were determined in Ribo-Calibration and BRIC-Seq data as described previously [26].

The translation initiation rate (I) for mitochondrial transcript k was defined as follows:

$$N_k = I_k R_k$$

where N_k and R_k represent the absolute mitoribosome number and the residence time of the loaded mitoribosome on transcript k, respectively. Since the loaded mitoribosome undergoes an elongation reaction on the ORF length L_k of transcript k, R_k was defined as follows:

$$R_k = L_k/E$$

where E represents the global mitochondrial elongation rate, which was determined to be 0.422 codon/s by mitoribosome run-off assay. Thus,

$$I_k = 0.422 N_k/L_k$$

The lifetime translation round (R) for mitochondrial transcript k was defined as follows:

$$R_k = I_k \int_0^{5T_k} \left(\frac{1}{2}\right)^{t/T_k} dt$$

where T_k represents the half-life of transcript k. The ribosome loading frequency was calculated as $5T_k$, when ~97% of the mRNA is predicted to be degraded.

To define mitochondrial translation initiation sites from retapamulin-assisted MitoIP-Thor-Ribo-Seq data, the A-site assigned reads at each nucleotide were normalized by the average reads per nucleotide of the transcript. The ROC curve was generated using the score at 13 annotated translation initiation sites as true positives. Then, the threshold was set at 99% specificity (1% false positive rate), which identified the peaks. We omitted the P sites within 3 nt upstream and 16 nt downstream of the annotated translation initiation sites. If the sites overlapped within 3 nt, the site with the highest value was chosen. We searched for possible AUG and AUA codons and their subcognates within a 5 nucleotide range (the peak position and 4 nt upstream). If those codons were not found, the 3 nt sequence upstream of the peak position was considered.

All custom scripts are available upon request.

Sucrose density gradient

The cell lysate (see section "*Standard Ribo-Seq and RNA-Seq*") or purified mitochondria fraction (see section "*MitoIP-Ribo-Seq, MitoIP-Thor-Ribo-Seq, and MitoIP-Thor-Disome-Seq*") was loaded onto a 10-50% sucrose gradient in SDG buffer (20 mM Tris-HCl pH 7.5, 150 mM NaCl, 5 mM $MgCl_2$, 1 mM DTT, and 100 μg/ml cycloheximide) and ultracentrifuged at 38,000 rpm and 4°C for 4 h by a Himac CP80WX ultracentrifuge (Hitachi) with a P40ST rotor (Hitachi). The gradients were fractionated with continuous

measurement of absorbance at 260 nm using a TRIAX flow cell (BioComp) and micro collector (ATTO).

On-gel mito-FUNCAT

On-gel mito-FUNCAT was performed as described previously [105,123]. HEK293 cells were cultured in a 6-well plate in methionine-free medium [DMEM, high glucose, no glutamine, no methionine, no cystine (Thermo Fisher Scientific), supplemented with 48 μg/ml L-cysteine and 4.08 mM L-alanyl-L-glutamine] with 50 μM homopropargylglycine (HPG) (Jena Bioscience) and 100 mg/ml anisomycin (Alomone Labs, A-520) for 3 h before cell harvest. During HPG labeling, cells were treated with the following compounds: tetracycline (5 μg/ml), chloramphenicol (100 μg/ml), fusidic acid (300 μg/ml), spectinomycin (300 μg/ml), hygromycin (300 μg/ml), G418 (150 μg/ml), kanamycin (60 μg/ml), streptomycin (300 μg/ml), capreomycin (300 μg/ml), blasticidin S (30 μg/ml), tigecycline (300 μg/ml), linezolid (300 μg/ml), thiostrepton (300 μg/ml), or retapamulin (100 μg/ml). An equivalent volume of solvent was used as a control for each compound. After washing with ice-cold PBS, cells were lysed with mito-FUNCAT lysis buffer (20 mM Tris-HCl pH 7.5, 150 mM NaCl, 5 mM $MgCl_2$, and 1% Triton X-100) and clarified by centrifugation at 20,000 × g for 10 min at 4°C. The HPG-labeled proteins in supernatants were labeled with 50 μM IRdye800CW Azide (LI-COR Biosciences) with a Click-it Cell Reaction Buffer Kit (Thermo Fisher Scientific) according to the manufacturer's instructions. The reactants were run on SDS–PAGE gels, and the specific signals were detected by an Odyssey CLx (LI-COR Biosciences) in the IR 800-nm channel. For standardization, the gels were stained with GelCode Blue Safe Protein Stain (Thermo Fisher Scientific) to monitor the protein input using the IR 700-

nm channel. The images were quantified with Image Studio (LI-COR Biosciences, version 5.2).

Western blotting

For Figure S1A, anti-MRPS22 (Thermo Fisher Scientific, PA5-52249, 1:1000) was used as a primary antibody, and IRDye800CW anti-rabbit IgG (LI-COR Biosciences, 926-32211, 1:10000) was used as a secondary antibody. Images were acquired with Odyssey CLx (LI-COR Biosciences) and Image Studio (LI-COR Biosciences, version 5.2).

For Figure S6A, anti-MTU1 antibody (Sigma–Aldrich, AV48819, 1:2000) and anti-VDAC [Cell Signaling Technology (CST), 4866, 1:2000] were used for primary antibodies, and anti-rabbit IgG, HRP-linked antibody (CST, 7074, 1:5000) was used as a secondary antibody. Antibodies were diluted with 5% skim milk (nacalai tesque, 31149-75) in PBS (Thermo Fisher Scientific, 10010023). Images were acquired with Fusion Solo S (VILBER).

Accession numbers

The results of MitoIP-Ribo-Seq, MitoIP-Thor-Ribo-Seq, standard Ribo-Seq, and RNA-Seq (GEO: GSE237154) obtained in this study have been deposited in the National Center for Biotechnology Information (NCBI) database. This study also used the reported data for standard Ribo-Seq, RNA-Seq, and BRIC-Seq (GSE233555 and GSE233374) [26].

Figure and table legends

Figure 1. Establishment of mitochondrial translation-tailored ribosome profiling with sample number scalability and low-input compatibility.

(A) Schematic of mitochondrial immunoprecipitation and subsequent ribosome profiling (MitoIP-Ribo-Seq).

(B) Sucrose density gradient ultracentrifugation for the separation of cytosolic and mitochondrial ribosome complexes.

(C) Periodicity scores (see Figure S1E-F for details) across the indicated conditions of MitoIP-Ribo-Seq.

(D) Metagene plots for the 5′ ends of 32 nt mitoribosome footprints around start codons (the first nucleotide of the start codon was set to 0) in MitoIP-Ribo-Seq (brown) and standard Ribo-Seq (black). *MT-ATP6* and *MT-ND4* were excluded from the analysis since their ORF start codons overlapped with *MT-ATP8* and *MT-ND4L*, respectively.

(E) Discrete Fourier transform of mitoribosome footprints around start codons.

(F-H) Plots of the 5′ ends of mitoribosome footprints along the length around start codons (the first nucleotide of the start codon was set to 0) for the indicated transcripts. The color scale indicates read abundance.

(I) Metagene plots for the 5′ ends of mitoribosome footprints along the length around stop codons (the first nucleotide of the stop codon was set to 0) for the transcripts whose stop codons were generated by poly(A) tailing. The color scale indicates the read abundance.

(J) Schematic representation of the relative position of the P site and A site on the mitoribosome footprints.

(K) Comparison of the fraction of mitochondrial transcript-mapped reads between our methods and published data.

RPM, reads per million mapped reads.

See also Figure S1 and Table S1.

Figure 2. Mitochondrial translation kinetics.

(A) Schematic of the mitoribosome run-off assay with retapamulin chase. After a short incubation with retapamulin, mitoribosomes preloaded on the transcripts were fixed by chloramphenicol.

(B) Smoothed metagene plots with footprints around start codons (the first nucleotide of the start codon was set to 0) in the mitoribosome run-off assay. *MT-ATP6* and *MT-ND4* were excluded from the analysis since their ORF start codons overlapped with *MT-ATP8* and *MT-ND4L*, respectively.

(C) The expansion of the mitoribosome-free area over time by retapamulin chase. Linear regression was used to determine the global elongation rates in mitochondria as 0.422 codon/s.

(D) The absolute mitoribosome number on the indicated transcripts, determined by Ribo-Calibration [26].

(E) The translation initiation rate of the indicated transcripts.

(F) The transcript half-life of the indicated transcripts, determined by BRIC-Seq [26].

(G) The lifetime translation rounds before transcript decay of the indicated transcripts.

(H) Schematic summary of mitochondrial translation kinetics parameters characterized in this study.

See also Figure S1 and Table S1.

Figure 3. Translation initiation survey by retapamulin-assisted MitoIP-Thor-Ribo-Seq.

(A-B and F-G) Distribution of mitoribosome footprints from retapamulin-treated and control cells along the indicated transcripts. The A-site position of each read is indicated. Codon sequences corresponding to the P site are highlighted. Magenta, annotated initiation sites; peacock green, cryptic initiation sites.

(C) The fraction of mitoribosome footprints along the read length for the indicated conditions.

(D-E) Pie charts for codon sequences of identified translation initiation sites (D) and their frame positions relative to the annotated ORFs (E).

See also Figure S2 and Table S1.

Figure 4. Translation regulation by f^5C modification, revealed by MitoIP-Thor-Ribo-Seq.

(A) Schematic of f^5C biosynthesis on mt-tRNA^{Met}.

(B) Mitoribosome occupancy change at A-site codons in *NSUN3* KO. AUA and AUG codons, which are recognized by mt-tRNA^{Met}, are highlighted.

(C) Mitoribosome occupancy of naïve and *NSUN3* KO cells for the indicated codons. The scores at each codon position (relative to the A site) are shown.

(D) Mitoribosome occupancy change at P-site AUA, A-site AUA, and PA-site AUA-AUA codons in *NSUN3* KO.

(E and G) Distribution of mitoribosome footprints from naïve and *NSUN3* KO cells along the indicated transcripts. The A-site position of each read is indicated. AUA codons are highlighted.

(F) Polarity scores (see Figure S3D) of the indicated transcripts in naïve and *NSUN3* KO cells. Data points from two replicates are shown individually.

(H) Mitoribosome occupancy change at P-site AUA, A-site AUA, and PA-site AUA-AUA codons in heart tissues from *Nsun3* KO mice.

(I) Distribution of mitoribosome footprints from hearts of wild-type and *Nsun*3 KO mice along the indicated transcripts. The A-site position of each read is indicated. AUA codons are highlighted.

(J) Translation efficiency measured by standard Ribo-Seq and RNA-Seq for mitochondrial transcripts. Transcripts are sorted according to their start codon sequences. RPM, reads per million mapped reads.

See also Figures S3 and S9 and Table S1.

Figure 5. Translation regulation by τm^5 modification, revealed by MitoIP-Thor-Ribo-Seq.

(A) Schematic of τm^5U34 biosynthesis on mt-tRNA$^{Leu\ (UUR)}$ and mt-tRNA^{Trp} and τm^5s^2U34 biosynthesis on mt-tRNA^{Lys}, mt-tRNA^{Gln}, and mt-tRNA^{Glu}.

(B-F and J) Mitoribosome occupancy of naïve and *GTPBP3* KO cells for the indicated codons. The scores at each codon position (relative to the A site) are shown.

(G and I) Distribution of mitoribosome footprints from naïve and *GTPBP3* KO cells along the indicated transcripts. The A-site position of each read is indicated. UUG, UGG, and AAG codons are highlighted.

(H) Polarity scores of the indicated transcripts in naïve and *GTPBP3* KO cells. Data points from two replicates are shown individually.

RPM, reads per million mapped reads.

See also Figures S4 and S9 and Table S1.

Figure 6. Translational dysregulation in MELAS patient cells with the A3243G mutation revealed by MitoIP-Thor-Ribo-Seq.

(A) Schematic of the A3243G mutation in mt-tRNA$^{Leu\ (UUR)}$.

(B) Mitoribosome occupancy of the indicated codons in naïve and A3243G myoblasts. The scores at each codon position (relative to the A site) are shown.

(C, F, and G) Distribution of mitoribosome footprints from naïve and A3243G myoblasts along the indicated transcripts. The A-site position of each read is indicated. UUG codons are highlighted.

(D) Metagene plots for mitoribosome footprints from naïve and A3243G myoblasts around UUG codons.

(E) Polarity scores of the indicated transcripts in naïve and A3243G myoblasts. Data points from two replicates are shown individually.

RPM, reads per million mapped reads.

See also Figures S5 and S9 and Table S1.

Figure 7. Translation regulation by s^2 modification, revealed by MitoIP-Thor-Ribo-Seq.

(A-D) Mitoribosome occupancy of the indicated codons in naïve and *MTU1* KO cells. The scores at each codon position (relative to the A site) are shown.

(E) Distribution of mitoribosome footprints along the indicated transcripts in naïve and *MTU1* KO cells. The A-site position of each read is indicated. GAG and GAC codons are highlighted.

RPM, reads per million mapped reads.

See also Figures S6 and S9 and Table S1.

Figure 8. Translation regulation by Q modification revealed by MitoIP-Thor-Ribo-Seq.

(A) Schematic of Q34 biosynthesis on mt-tRNA^{Asn}, mt-tRNA^{His}, mt-tRNA^{Asp}, and mt-tRNA^{Tyr}.

(B and C) Mitoribosome occupancy change at A-site U-ending codons (B; AAU, CAU, GAU, and UAU) and C-ending codons (C; AAC, CAC, GAC, and UAC) in *QTRT1* KO and *QTRT2* KO. Codons with statistically significant changes in both *QTRT1* KO and *QTRT2* KO are highlighted.

See also Figures S7 and S9 and Table S1.

Figure 9. Translation regulation by t^{6}A modification revealed by MitoIP-Thor-Ribo-Seq.

(A) Schematic of t^{6}A37 biosynthesis on mt-tRNA^{Lys}, mt-tRNA^{Asn}, mt-tRNA^{Thr}, mt-tRNA^{Ile}, and mt-tRNA$^{Ser\ (AGY)}$.

(B-G and K) Mitoribosome occupancy of naïve and *OSGEPL1* KO cells for the indicated codons. The scores at each codon position (relative to the A site) are shown.

(H and J) Distribution of mitoribosome footprints from naïve and *OSGEPL1* KO cells along the indicated transcripts. The A-site position of each read is indicated. AAG codons are highlighted.

(I) Polarity scores of the indicated transcripts in naïve and *OSGEPL1* KO cells. Data points from two replicates are shown individually.

RPM, reads per million mapped reads.

See also Figures S8 and S9 and Table S1.

Figure 10. Mitoribosome pause sites revealed by MitoIP-Thor-Disome-Seq.

(A) Schematic of mitochondrial disome profiling.

(B) Plots for the 5′ ends of mito-disome footprints around AUA-AUA (312-313, counting the first nucleotide of start codon as position 0) dicodons in *MT-NT5* in naïve and *NSUN3* KO cells. The color scale indicates the read abundance.

(C) Schematic representation of the relative position of the A site in the leading paused mitoribosome for mito-disome footprints.

(D) Relative abundance of mito-disome footprints over mito-monosome footprints on the indicated transcripts. Data include the reads from overlapping ORF regions in *MT-ATP8*/*MT-ATP6* and *MT-ND4L*/*MT-ND4*.

(E-G) Distribution of mito-monosome and mito-disome footprints from naïve cells along the indicated transcripts. The A-site position (in the case of mito-disomes, the leading paused mitoribosome) of each read is indicated. The AGA stop codon is highlighted.

(H) Schematic of configurations of mito-disome pause sites found in *MT-CO1*, *MT-CO3*, and *MT-CYB* with the cotranslational membrane insertion of their nascent peptides.

(I) Schematic of mitoribosome collision around the noncanonical AGA stop codon associated with inefficient termination and recycling reactions.

RPM, reads per million mapped reads.

See also Figure S10 and Table S1.

Figure S1. Optimization of MitoIP-Ribo-Seq, related to Figures 1 and 2.

(A) Western blotting of MRPS22/mS22 to evaluate mitoribosome isolation. The RNase I-treated (0.2 U) lysate (or input) were subjected to sucrose cushion ultracentrifugation or size-exclusion gel-filtration spin column.

(B) The fraction of mitoribosome footprints and relative entropy (Kullback–Leibler divergence) along the read length for the indicated conditions.

(C) On-gel mitochondrial-specific fluorescent noncanonical amino acid tagging (on-gel mito-FUNCAT) to test the effect of the indicated bacterial ribosome inhibitors on mitochondrial translation.

(D) The combination of the conventional rRNA subtraction method (Ribo-Zero) with Ribo-FilterOut [26] in standard Ribo-Seq. Reads mapped to mitochondrial transcripts were analyzed.

(E and F) Schematic of the calculation of relative entropy (Kullback–Leibler divergence) (E) and the definition of the periodicity score (F).

(G-I) Plots of the 5′ ends of mitoribosome footprints along the length around start codons (the first nucleotide of the start codon was set to 0) for the indicated transcripts. The color scale indicates the read abundance.

(J) Metagene plots for the 5′ ends of mitoribosome footprints around stop codons (the first nucleotide of the stop codon was set to 0). *MT-ATP8* and *MT-ND4L* were excluded from the analysis since their ORF stop codons overlapped with *MT-ATP6* and *MT-ND4,* respectively. *MT-CO1* and *MT-ND6* were also excluded from the analysis since they possess noncanonical stop codons (AGA and AGG).

(K) Mitoribosome occupancy at the A site, P site, or E site for MitoIP-Ribo-Seq (top) and MitoIP-Thor-Ribo-Seq (bottom). Data for the codon sequence (left) and amino acid sequence (right) are shown. The color scale indicates the mitoribosome occupancy.

(L) The fraction of mitoribosome footprints along the read length for the indicated conditions.

(M) The distance between mitoribosomes on the indicated transcripts, determined by Ribo-Calibration [26].

RPM, reads per million mapped reads.

Figure S2. Characterization of retapamulin-assisted MitoIP-Thor-Ribo-Seq, related to Figure 3.

(A) Schematic of the peak calling with threshold setting.

(B) ROC curve to determine the threshold for the peak calling. The relative read counts at the annotated translation initiation sites were used as true positives. The cutoff point used for this analysis is highlighted.

(C-I) Distribution of mitoribosome footprints along the indicated transcripts in retapamulin-treated and control cells. The A-site position of each read is indicated. Codon sequences corresponding to the P site are highlighted. Magenta, annotated initiation sites; peacock green, cryptic initiation sites.

RPM, reads per million mapped reads.

Figure S3. Characterization of MitoIP-Thor-Ribo-Seq for *NSUN3* KO cells, related to Figure 4.

(A) Schematic of the modified nucleotide positions on mt-tRNA investigated in this study.

(B and E) The fraction of mitoribosome footprints along the read length for the indicated conditions.

(C) Mitoribosome occupancy change at P-site codons in *NSUN3* KO cells. AUA and AUG codons, which are recognized by mt-tRNA^{Met,} are highlighted. We note that footprints at the start codon on P site were excluded from this analysis.

(D) Schematic of the polarity score of mitoribosome footprints.

(F and G) Plots for the 5′ ends of mitoribosome footprints around start codons (the first nucleotide of the start codon was set to 0) for the indicated transcripts. The color scale indicates the read abundance.

(H) Polarity scores of the indicated transcripts in the hearts of wild-type and *Nsun*3 KO mice. Data points from two replicates are shown individually.

(I) Distribution of mitoribosome footprints along the indicated transcripts in heart tissues from wild-type and *Nsun*3 KO mice. The A-site position of each read is indicated. AUA codons are highlighted.

RPM, reads per million mapped reads.

Figure S4. Characterization of MitoIP-Thor-Ribo-Seq for *GTPBP3* KO cells, related to Figure 5.

(A) The fraction of mitoribosome footprints along the read length for the indicated conditions.

(B) Mitoribosome occupancy of naïve and *GTPBP3* KO cells for the indicated codons. The scores at each codon position (relative to the A site) are shown.

Figure S5. Characterization of MitoIP-Thor-Ribo-Seq for A3243G myoblasts, related to Figure 6.

(A) The fraction of mitoribosome footprints along the read length for the indicated conditions.

(B) Metagene plots for mitoribosome footprints from naïve and A3243G myoblasts around UUA codons.

Figure S6. Characterization of MitoIP-Thor-Ribo-Seq for *MTU1* KO cells, related to Figure 7.

(A) The loss of MTU1 protein in *MTU1* KO cells was validated by Western blotting. Each lane represents a biological replicate. VDAC, a mitochondrial membrane protein, was detected as a loading control.

(B) The loss of mitochondrial tRNA 2-thiolation was investigated with mass spectrometry. τm^5s^2U modification disappeared in the total RNA purified from *MTU1* KO cells, whereas ms^2i^6A, a mitochondrial tRNA-specific modification, remained intact.

(C) The fraction of mitoribosome footprints along the read length for the indicated conditions.

(D) Polarity scores of the indicated transcripts in naïve and *MTU1* KO cells. Data points from two replicates are shown individually.

Figure S7. Characterization of MitoIP-Thor-Ribo-Seq for *QTRT1* KO and *QTRT2* KO cells, related to Figure 8.

(A) The fraction of mitoribosome footprints along the read length for the indicated conditions.

(B) Polarity scores of the indicated transcripts in naïve, *QTRT1* KO, and *QTRT2* KO cells. Data points from two replicates are shown individually.

(C and D) Mitoribosome occupancy change at P-site U-ending codons (C; AAU, CAU, GAU, and UAU) and C-ending codons (D; AAC, CAC, GAC, and UAC) in *QTRT1* KO and *QTRT2* KO cells. Codons with statistically significant changes in both *QTRT1* KO and *QTRT2* KO are highlighted.

Figure S8. Characterization of MitoIP-Thor-Ribo-Seq for *OSGEPL1* KO cells, related to Figure 9.

(A) The fraction of mitoribosome footprints along the read length for the indicated conditions.

(B) Metagene plots for mitoribosome footprints from naïve and *OSGEPL1* KO cells around stop codons. *MT-ATP8* and *MT-ND4L* were excluded from the analysis since their ORF stop codons overlapped with *MT-ATP6* and *MT-ND4,* respectively. *MT-CO1* and *MT-ND6* were also excluded from the analysis since they possess noncanonical stop codons (AGA and AGG).

Figure S9. Summary of the impact of mt-tRNA modification on translation elongation in mitochondria, related to Figures 4-9.

The color represents the indicated modifications and the effects on mitoribosome traversal on each codon.

Figure S10. Characterization of MitoIP-Thor-Disome-Seq, related to Figure 10.

(A) The fraction of mito-monosome and mito-disome footprints along the read length for the indicated conditions. The mito-monosome data are the same as those shown in Figure S3B.

(B-D) Distribution of mito-monosome (C) and mito-disome (B and D) footprints along the indicated transcripts from naïve and *NSUN3* KO cells. The A-site position (in the case of mito-disome, the leading paused mitoribosome) of each read is indicated. AUA codons are highlighted.

(E and F) Comparison of mito-monosome (F) and mito-disome (E) occupancy at A-site codons under the indicated conditions.

(G-H) Distribution of mito-monosome and mito-disome footprints along the indicated transcripts from naïve cells. The A-site position (in the case of mito-disome, the leading paused mitoribosome) of each read is indicated .

(I) Schematic of configurations of mito-disome pause sites found in *MT-ND6* and *MT-ATP8/ATP6* with the cotranslational membrane insertion of their nascent peptides.

(J) mRNA expression of nuclear genome-encoded genes and mitochondrial genome-encoded genes.

RPM, reads per million mapped reads; TPM, transcripts per million.

Table S1. Summary of deep sequencing data used in this study, related to Figure 1-10.

For each data set, the library name, treatment, species name, cell line or strain name, rRNA depletion method, Ribo-Calibration application, replicate number, data type, RNA-Seq kit name, input amount, reference, and accession number are listed.

References

1. Kummer, E. & Ban, N. Mechanisms and regulation of protein synthesis in mitochondria. *Nat. Rev. Mol. Cell Biol.* **22**, 307–325 (2021).
2. Aitken, C. E. & Lorsch, J. R. A mechanistic overview of translation initiation in eukaryotes. *Nat. Struct. Mol. Biol.* **19**, 568–576 (2012).
3. Sokabe, M. & Fraser, C. S. Toward a kinetic understanding of eukaryotic translation. *Cold Spring Harb. Perspect. Biol.* **11**, (2019).
4. Anderson, S. *et al.* Sequence and organization of the human mitochondrial genome. *Nature* **290**, 457–465 (1981).
5. Ruiz-Pesini, E. *et al.* An enhanced MITOMAP with a global mtDNA mutational phylogeny. *Nucleic Acids Res.* **35**, D823–8 (2007).
6. Gorman, G. S. *et al.* Mitochondrial diseases. *Nat Rev Dis Primers* **2**, 16080 (2016).
7. Suomalainen, A. & Battersby, B. J. Mitochondrial diseases: the contribution of organelle stress responses to pathology. *Nat. Rev. Mol. Cell Biol.* **19**, 77–92 (2018).
8. Apostolopoulos, A. & Iwasaki, S. Into the matrix: current methods for mitochondrial translation studies. *J. Biochem.* **171**, 379–387 (2022).
9. Ingolia, N. T., Ghaemmaghami, S., Newman, J. R. & Weissman, J. S. Genome-wide analysis *in vivo* of translation with nucleotide resolution using ribosome profiling. *Science* **324**, 218–223 (2009).
10. Rooijers, K., Loayza-Puch, F., Nijtmans, L. G. & Agami, R. Ribosome profiling reveals features of normal and disease-associated mitochondrial translation. *Nat. Commun.* **4**, 2886 (2013).
11. Pearce, S. F. *et al.* Maturation of selected human mitochondrial tRNAs requires

deadenylation. *Elife* **6**, e27596 (2017).

12. Gao, F. *et al.* Using mitoribosomal profiling to investigate human mitochondrial translation. *Wellcome Open Res* **2**, 116 (2017).
13. Morscher, R. J. *et al.* Mitochondrial translation requires folate-dependent tRNA methylation. *Nature* **554**, 128–132 (2018).
14. Li, S. H.-J., Nofal, M., Parsons, L. R., Rabinowitz, J. D. & Gitai, Z. Monitoring mammalian mitochondrial translation with MitoRiboSeq. *Nat. Protoc.* **16**, 2802–2825 (2021).
15. Schöller, E. *et al.* Balancing of mitochondrial translation through METTL8-mediated m^3C modification of mitochondrial tRNAs. *Mol. Cell* **81**, 4810–4825.e12 (2021).
16. Soto, I. *et al.* Balanced mitochondrial and cytosolic translatomes underlie the biogenesis of human respiratory complexes. *Genome Biol.* **23**, 170 (2022).
17. Tatavarty, V. *et al.* Single-molecule imaging of translational output from individual RNA granules in neurons. *Mol. Biol. Cell* **23**, 918–929 (2012).
18. Morisaki, T. *et al.* Real-time quantification of single RNA translation dynamics in living cells. *Science* **352**, 1425–1429 (2016).
19. Wu, B., Eliscovich, C., Yoon, Y. J. & Singer, R. H. Translation dynamics of single mRNAs in live cells and neurons. *Science* **352**, 1430–1435 (2016).
20. Yan, X., Hoek, T. A., Vale, R. D. & Tanenbaum, M. E. Dynamics of translation of single mRNA molecules *in vivo*. *Cell* **165**, 976–989 (2016).
21. Wang, C., Han, B., Zhou, R. & Zhuang, X. Real-time imaging of translation on single mRNA transcripts in live cells. *Cell* **165**, 990–1001 (2016).
22. Voigt, F. *et al.* Single-molecule quantification of translation-dependent association

of mRNAs with the endoplasmic reticulum. *Cell Rep.* **21**, 3740–3753 (2017).

23. Livingston, N. M. *et al.* Bursting translation on single mRNAs in live cells. *Mol. Cell* **83**, 2276–2289.e11 (2023).
24. Gerashchenko, M. V., Peterfi, Z., Yim, S. H. & Gladyshev, V. N. Translation elongation rate varies among organs and decreases with age. *Nucleic Acids Res.* **49**, e9 (2021).
25. Ingolia, N. T., Lareau, L. F. & Weissman, J. S. Ribosome profiling of mouse embryonic stem cells reveals the complexity and dynamics of mammalian proteomes. *Cell* **147**, 789–802 (2011).
26. Tomuro, K. *et al.* Absolute calibration of ribosome profiling assesses the dynamics of ribosomal flux on transcripts. *bioRxiv* (2023) doi:10.1101/2023.06.20.545829.
27. Mito, M., Shichino, Y. & Iwasaki, S. Thor-Ribo-Seq: ribosome profiling tailored for low input with RNA-dependent RNA amplification. *bioRxiv* 2023.01.15.524129 (2023) doi:10.1101/2023.01.15.524129.
28. Mito, M., Mishima, Y. & Iwasaki, S. Protocol for disome profiling to survey ribosome collision in humans and zebrafish. *STAR Protoc* **1**, 100168 (2020).
29. Gerashchenko, M. V. & Gladyshev, V. N. Ribonuclease selection for ribosome profiling. *Nucleic Acids Res.* **45**, e6 (2017).
30. Liu, B. *et al.* Optimization of ribosome profiling using low-input brain tissue from fragile X syndrome model mice. *Nucleic Acids Res.* **47**, e25 (2019).
31. Martinez, T. F. *et al.* Accurate annotation of human protein-coding small open reading frames. *Nat. Chem. Biol.* **16**, 458–468 (2020).
32. Li, Q., Yang, H., Stroup, E. K., Wang, H. & Ji, Z. Low-input RNase footprinting for simultaneous quantification of cytosolic and mitochondrial translation. *Genome*

Res. **32**, 545–557 (2022).

33. Gerashchenko, M. V. & Gladyshev, V. N. Translation inhibitors cause abnormalities in ribosome profiling experiments. *Nucleic Acids Res.* **42**, e134 (2014).
34. Lareau, L. F., Hite, D. H., Hogan, G. J. & Brown, P. O. Distinct stages of the translation elongation cycle revealed by sequencing ribosome-protected mRNA fragments. *Elife* **3**, e01257 (2014).
35. Hussmann, J. A., Patchett, S., Johnson, A., Sawyer, S. & Press, WH. Understanding biases in ribosome profiling experiments reveals signatures of translation dynamics in yeast. *PLoS Genet.* **11**, e1005732 (2015).
36. Santos, D. A., Shi, L., Tu, B. P. & Weissman, J. S. Cycloheximide can distort measurements of mRNA levels and translation efficiency. *Nucleic Acids Res.* **47**, 4974–4985 (2019).
37. Duncan, C. D. S. & Mata, J. Effects of cycloheximide on the interpretation of ribosome profiling experiments in *Schizosaccharomyces pombe*. *Sci. Rep.* **7**, 10331 (2017).
38. Wu, C. C., Zinshteyn, B., Wehner, K. A. & Green, R. High-resolution ribosome profiling defines discrete ribosome elongation states and translational regulation during cellular stress. *Mol. Cell* **73**, 959–970.e5 (2019).
39. Sharma, P., Wu, J., Nilges, B. S. & Leidel, S. A. Humans and other commonly used model organisms are resistant to cycloheximide-mediated biases in ribosome profiling experiments. *Nat. Commun.* **12**, 5094 (2021).
40. Ingolia, N. T., Brar, G. A., Rouskin, S., McGeachy, A. M. & Weissman, J. S. The ribosome profiling strategy for monitoring translation *in vivo* by deep sequencing

of ribosome-protected mRNA fragments. *Nat. Protoc.* **7**, 1534–1550 (2012).

41. Temperley, R. J., Wydro, M., Lightowlers, R. N. & Chrzanowska-Lightowlers, Z. M. Human mitochondrial mRNAs—like members of all families, similar but different. *Biochimica et Biophysica Acta (BBA) - Bioenergetics* **1797**, 1081–1085 (2010).
42. Marks, J. *et al.* Context-specific inhibition of translation by ribosomal antibiotics targeting the peptidyl transferase center. *Proc. Natl. Acad. Sci. U. S. A.* **113**, 12150–12155 (2016).
43. Mohammad, F., Green, R. & Buskirk, A. R. A systematically-revised ribosome profiling method for bacteria reveals pauses at single-codon resolution. *Elife* **8**, e42591 (2019).
44. Syroegin, E. A. *et al.* Structural basis for the context-specific action of the classic peptidyl transferase inhibitor chloramphenicol. *Nat. Struct. Mol. Biol.* **29**, 152–161 (2022).
45. Tsai, K. *et al.* Structural basis for context-specific inhibition of translation by oxazolidinone antibiotics. *Nat. Struct. Mol. Biol.* **29**, 162–171 (2022).
46. Shichino, Y. & Iwasaki, S. Compounds for selective translational inhibition. *Curr. Opin. Chem. Biol.* **69**, 102158 (2022).
47. Meydan, S. *et al.* Retapamulin-assisted ribosome profiling reveals the alternative bacterial proteome. *Mol. Cell* **74**, 481–493.e6 (2019).
48. Tani, H. *et al.* Genome-wide determination of RNA stability reveals hundreds of short-lived noncoding transcripts in mammals. *Genome Res.* **22**, 947–956 (2012).
49. Paulsen, M. T. *et al.* Coordinated regulation of synthesis and stability of RNA during the acute TNF-induced proinflammatory response. *Proc. Natl. Acad. Sci. U.*

S. A. **110**, 2240–2245 (2013).

50. Chujo, T. *et al.* LRPPRC/SLIRP suppresses PNPase-mediated mRNA decay and promotes polyadenylation in human mitochondria. *Nucleic Acids Res.* **40**, 8033–8047 (2012).
51. Lee, S. *et al.* Global mapping of translation initiation sites in mammalian cells at single-nucleotide resolution. *Proc. Natl. Acad. Sci. U. S. A.* **109**, E2424–32 (2012).
52. Gao, X. *et al.* Quantitative profiling of initiating ribosomes in vivo. *Nat. Methods* **12**, 147–153 (2015).
53. Nakano, S. *et al.* NSUN3 methylase initiates 5-formylcytidine biogenesis in human mitochondrial $tRNA^{Met}$. *Nat. Chem. Biol.* **12**, 546–551 (2016).
54. Haag, S. *et al.* NSUN3 and ABH1 modify the wobble position of mt-$tRNA^{Met}$ to expand codon recognition in mitochondrial translation. *EMBO J.* **35**, 2104–2119 (2016).
55. Van Haute, L. *et al.* Deficient methylation and formylation of mt-$tRNA^{Met}$ wobble cytosine in a patient carrying mutations in NSUN3. *Nat. Commun.* **7**, 12039 (2016).
56. Kawarada, L. *et al.* ALKBH1 is an RNA dioxygenase responsible for cytoplasmic and mitochondrial tRNA modifications. *Nucleic Acids Res.* **45**, 7401–7415 (2017).
57. Takemoto, C. *et al.* Unconventional decoding of the AUA codon as methionine by mitochondrial $tRNA^{Met}$ with the anticodon f^5CAU as revealed with a mitochondrial *in vitro* translation system. *Nucleic Acids Res.* **37**, 1616–1627 (2009).
58. Cantara, W. A., Murphy, F. V., 4th, Demirci, H. & Agris, P. F. Expanded use of sense codons is regulated by modified cytidines in tRNA. *Proc. Natl. Acad. Sci. U. S. A.* **110**, 10964–10969 (2013).
59. Schuller, A. P., Wu, C. C., Dever, T. E., Buskirk, A. R. & Green, R. eIF5A

functions globally in translation elongation and termination. *Mol. Cell* **66**, 194–205.e5 (2017).

60. Murakami, Y. *et al.* NSUN3-mediated mitochondrial tRNA 5-formylcytidine modification is essential for embryonic development and respiratory complexes in mice. *Commun Biol* **6**, 307 (2023).
61. Suzuki, T. The expanding world of tRNA modifications and their disease relevance. *Nat. Rev. Mol. Cell Biol.* **22**, 375–392 (2021).
62. Suzuki, T., Suzuki, T., Wada, T., Saigo, K. & Watanabe, K. Taurine as a constituent of mitochondrial tRNAs: new insights into the functions of taurine and human mitochondrial diseases. *EMBO J.* **21**, 6581–6589 (2002).
63. Umeda, N. *et al.* Mitochondria-specific RNA-modifying enzymes responsible for the biosynthesis of the wobble base in mitochondrial tRNAs. Implications for the molecular pathogenesis of human mitochondrial diseases. *J. Biol. Chem.* **280**, 1613–1624 (2005).
64. Asano, K. *et al.* Metabolic and chemical regulation of tRNA modification associated with taurine deficiency and human disease. *Nucleic Acids Res.* **46**, 1565–1583 (2018).
65. Fakruddin, M. *et al.* Defective mitochondrial tRNA taurine modification activates global proteostress and leads to mitochondrial disease. *Cell Rep.* **22**, 482–496 (2018).
66. Zeharia, A. *et al.* Acute infantile liver failure due to mutations in the *TRMU* gene. *Am. J. Hum. Genet.* **85**, 401–407 (2009).
67. Wu, Y. *et al.* Mtu1-mediated thiouridine formation of mitochondrial tRNAs is required for mitochondrial translation and is involved in reversible infantile liver

injury. *PLoS Genet.* **12**, e1006355 (2016).

68. Zhang, Q. *et al.* Deletion of Mtu1 (Trmu) in zebrafish revealed the essential role of tRNA modification in mitochondrial biogenesis and hearing function. *Nucleic Acids Res.* **46**, 10930–10945 (2018).
69. Suzuki, T. *et al.* Complete chemical structures of human mitochondrial tRNAs. *Nat. Commun.* **11**, 4269 (2020).
70. Goto, Y., Nonaka, I. & Horai, S. A mutation in the $tRNA^{Leu(UUR)}$ gene associated with the MELAS subgroup of mitochondrial encephalomyopathies. *Nature* **348**, 651–653 (1990).
71. Goto, Y., Nonaka, I. & Horai, S. A new mtDNA mutation associated with mitochondrial myopathy, encephalopathy, lactic acidosis and stroke-like episodes (MELAS). *Biochim. Biophys. Acta* **1097**, 238–240 (1991).
72. Kobayashi, Y. *et al.* A point mutation in the mitochondrial $tRNA^{Leu(UUR)}$ gene in MELAS (mitochondrial myopathy, encephalopathy, lactic acidosis and stroke-like episodes). *Biochem. Biophys. Res. Commun.* **173**, 816–822 (1990).
73. Sohm, B. *et al.* Towards understanding human mitochondrial leucine aminoacylation identity. *J. Mol. Biol.* **328**, 995–1010 (2003).
74. Sohm, B., Sissler, M., Park, H., King, M. P. & Florentz, C. Recognition of human mitochondrial $tRNA^{Leu(UUR)}$ by its cognate leucyl-tRNA synthetase. *J. Mol. Biol.* **339**, 17–29 (2004).
75. Yasukawa, T., Suzuki, T., Ueda, T., Ohta, S. & Watanabe, K. Modification defect at anticodon wobble nucleotide of mitochondrial $tRNAs^{Leu(UUR)}$ with pathogenic mutations of mitochondrial myopathy, encephalopathy, lactic acidosis, and stroke-like episodes. *J. Biol. Chem.* **275**, 4251–4257 (2000).

76. Kirino, Y., Goto, Y.-I., Campos, Y., Arenas, J. & Suzuki, T. Specific correlation between the wobble modification deficiency in mutant tRNAs and the clinical features of a human mitochondrial disease. *Proc. Natl. Acad. Sci. U. S. A.* **102**, 7127–7132 (2005).

77. Tomoda, E. *et al.* Restoration of mitochondrial function through activation of hypomodified tRNAs with pathogenic mutations associated with mitochondrial diseases. *Nucleic Acids Res.* (2023) doi:10.1093/nar/gkad139.

78. Sasarman, F., Antonicka, H. & Shoubridge, E. A. The A3243G $tRNA^{Leu(UUR)}$ MELAS mutation causes amino acid misincorporation and a combined respiratory chain assembly defect partially suppressed by overexpression of EFTu and EFG2. *Hum. Mol. Genet.* **17**, 3697–3707 (2008).

79. Kirino, Y. *et al.* Codon-specific translational defect caused by a wobble modification deficiency in mutant tRNA from a human mitochondrial disease. *Proc. Natl. Acad. Sci. U. S. A.* **101**, 15070–15075 (2004).

80. Tuorto, F. *et al.* Queuosine-modified tRNAs confer nutritional control of protein translation. *EMBO J.* **37**, e99777 (2018).

81. Chen, Y.-C., Kelly, V. P., Stachura, S. V. & Garcia, G. A. Characterization of the human tRNA-guanine transglycosylase: confirmation of the heterodimeric subunit structure. *RNA* **16**, 958–968 (2010).

82. Björk, G. R., Wikström, P. M. & Byström, A. S. Prevention of translational frameshifting by the modified nucleoside 1-methylguanosine. *Science* **244**, 986–989 (1989).

83. Han, L. & Phizicky, E. M. A rationale for tRNA modification circuits in the anticodon loop. *RNA* **24**, 1277–1284 (2018).

84. Lin, H. *et al.* CO_2-sensitive tRNA modification associated with human mitochondrial disease. *Nat. Commun.* **9**, 1–17 (2018).

85. Jia, L. *et al.* Yeast Oxa1 interacts with mitochondrial ribosomes: the importance of the C-terminal region of Oxa1. *EMBO J.* **22**, 6438–6447 (2003).

86. Szyrach, G., Ott, M., Bonnefoy, N., Neupert, W. & Herrmann, J. M. Ribosome binding to the Oxa1 complex facilitates co-translational protein insertion in mitochondria. *EMBO J.* **22**, 6448–6457 (2003).

87. Haque, M. E. *et al.* Properties of the C-terminal tail of human mitochondrial inner membrane protein Oxa1L and its interactions with mammalian mitochondrial ribosomes. *J. Biol. Chem.* **285**, 28353–28362 (2010).

88. Ott, M. *et al.* Mba1, a membrane-associated ribosome receptor in mitochondria. *EMBO J.* **25**, 1603–1610 (2006).

89. Pfeffer, S., Woellhaf, M. W., Herrmann, J. M. & Förster, F. Organization of the mitochondrial translation machinery studied in situ by cryoelectron tomography. *Nat. Commun.* **6**, 6019 (2015).

90. Englmeier, R., Pfeffer, S. & Förster, F. Structure of the human mitochondrial ribosome studied *in situ* by cryoelectron tomography. *Structure* **25**, 1574–1581.e2 (2017).

91. Itoh, Y. *et al.* Mechanism of membrane-tethered mitochondrial protein synthesis. *Science* **371**, 846–849 (2021).

92. Richter-Dennerlein, R. *et al.* Mitochondrial protein synthesis adapts to influx of nuclear-encoded protein. *Cell* **167**, 471–483.e10 (2016).

93. Guydosh, N. R. & Green, R. Dom34 rescues ribosomes in 3′ untranslated regions. *Cell* **156**, 950–962 (2014).

94. Subramaniam, A. R., Zid, B. M. & O'Shea, E. K. An integrated approach reveals regulatory controls on bacterial translation elongation. *Cell* **159**, 1200–1211 (2014).

95. Diament, A. *et al.* The extent of ribosome queuing in budding yeast. *PLoS Comput. Biol.* **14**, e1005951 (2018).

96. Arpat, A. B. *et al.* Transcriptome-wide sites of collided ribosomes reveal principles of translational pausing. *Genome Res.* **30**, 985–999 (2020).

97. Han, P. *et al.* Genome-wide survey of ribosome collision. *Cell Rep.* **31**, 107610 (2020).

98. Meydan, S. & Guydosh, N. R. Disome and trisome profiling reveal genome-wide targets of ribosome quality control. *Mol. Cell* **79**, 588–602.e6 (2020).

99. Tuck, A. C. *et al.* Mammalian RNA decay pathways are highly specialized and widely linked to translation. *Mol. Cell* **77**, 1222–1236.e13 (2020).

100. Bhatt, P. R. *et al.* Structural basis of ribosomal frameshifting during translation of the SARS-CoV-2 RNA genome. *Science* **372**, 1306–1313 (2021).

101. Kim, E. Y. *et al.* Ribosome stalling and SGS3 phase separation prime the epigenetic silencing of transposons. *Nat Plants* **7**, 303–309 (2021).

102. Zhao, T. *et al.* Disome-seq reveals widespread ribosome collisions that promote cotranslational protein folding. *Genome Biol.* **22**, 16 (2021).

103. Fujita, T. *et al.* The landscape of translational stall sites in bacteria revealed by monosome and disome profiling. *RNA* **28**, 290–302 (2022).

104. Morisaki, T. & Stasevich, T. J. Quantifying Single mRNA Translation Kinetics in Living Cells. *Cold Spring Harb. Perspect. Biol.* **10**, (2018).

105. Kimura, Y. *et al.* Mito-FUNCAT-FACS reveals cellular heterogeneity in mitochondrial translation. *RNA* **28**, 895–904 (2022).

106. Vinayak, M. & Pathak, C. Queuosine modification of tRNA: its divergent role in cellular machinery. *Biosci. Rep.* **30**, 135–148 (2009).

107. Fergus, C., Barnes, D., Alqasem, M. A. & Kelly, V. P. The queuine micronutrient: charting a course from microbe to man. *Nutrients* **7**, 2897–2929 (2015).

108. Zinshteyn, B. & Gilbert, W. V. Loss of a conserved tRNA anticodon modification perturbs cellular signaling. *PLoS Genet.* **9**, e1003675 (2013).

109. Nedialkova, D. D. & Leidel, S. A. Optimization of codon translation rates via tRNA modifications maintains proteome integrity. *Cell* **161**, 1606–1618 (2015).

110. Chou, H.-J., Donnard, E., Gustafsson, H. T., Garber, M. & Rando, O. J. Transcriptome-wide analysis of roles for tRNA modifications in translational regulation. *Mol. Cell* **68**, 978–992.e4 (2017).

111. Thiaville, P. C. *et al.* Global translational impacts of the loss of the tRNA modification t^6A in yeast. *Microb. Cell Fact.* **3**, 29–45 (2016).

112. Lin, C. A., Ellis, S. R. & True, H. L. The Sua5 protein is essential for normal translational regulation in yeast. *Mol. Cell. Biol.* **30**, 354–363 (2010).

113. Remes, C. *et al.* Translation initiation of leaderless and polycistronic transcripts in mammalian mitochondria. *Nucleic Acids Res.* **51**, 891–907 (2023).

114. Cruz-Zaragoza, L. D. *et al.* An *in vitro* system to silence mitochondrial gene expression. *Cell* **184**, 5824–5837.e15 (2021).

115. Hickey, K. L. *et al.* GIGYF2 and 4EHP inhibit translation initiation of defective messenger RNAs to assist ribosome-associated quality control. *Mol. Cell* **79**, 950–962.e6 (2020).

116. Sanjana, N. E., Shalem, O. & Zhang, F. Improved vectors and genome-wide libraries for CRISPR screening. *Nat. Methods* **11**, 783–784 (2014).

117. Kashiwagi, K. *et al.* eIF2B-capturing viral protein NSs suppresses the integrated stress response. *Nat. Commun.* **12**, 7102 (2021).

118. McGlincy, N. J. & Ingolia, N. T. Transcriptome-wide measurement of translation by ribosome profiling. *Methods* **126**, 112–129 (2017).

119. Chen, S., Zhou, Y., Chen, Y. & Gu, J. fastp: an ultra-fast all-in-one FASTQ preprocessor. *Bioinformatics* **34**, i884–i890 (2018).

120. Dobin, A. *et al.* STAR: ultrafast universal RNA-seq aligner. *Bioinformatics* **29**, 15–21 (2013).

121. Smith, T., Heger, A. & Sudbery, I. UMI-tools: modeling sequencing errors in Unique Molecular Identifiers to improve quantification accuracy. *Genome Res.* **27**, 491–499 (2017).

122. Love, M. I., Huber, W. & Anders, S. Moderated estimation of fold change and dispersion for RNA-seq data with DESeq2. *Genome Biol.* **15**, 550 (2014).

123. Wakigawa, T. *et al.* Gravitational and mechanical forces drive mitochondrial translation through the cell adhesion–FAK axis. *bioRxiv* 2023.01.18.524628 (2023) doi:10.1101/2023.01.18.524628.

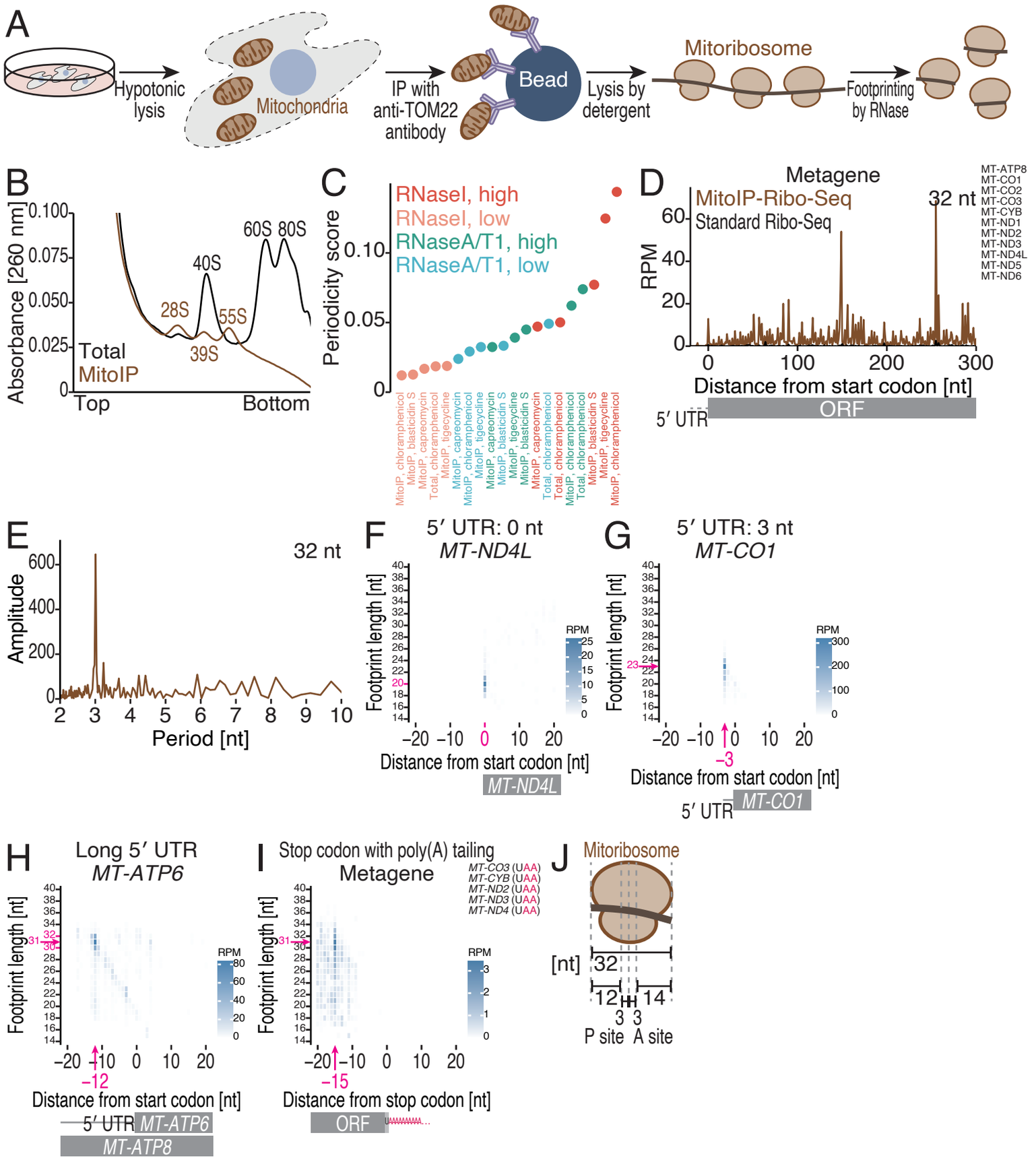

Figure 1 Wakigawa, Mito *et al.* (2023)

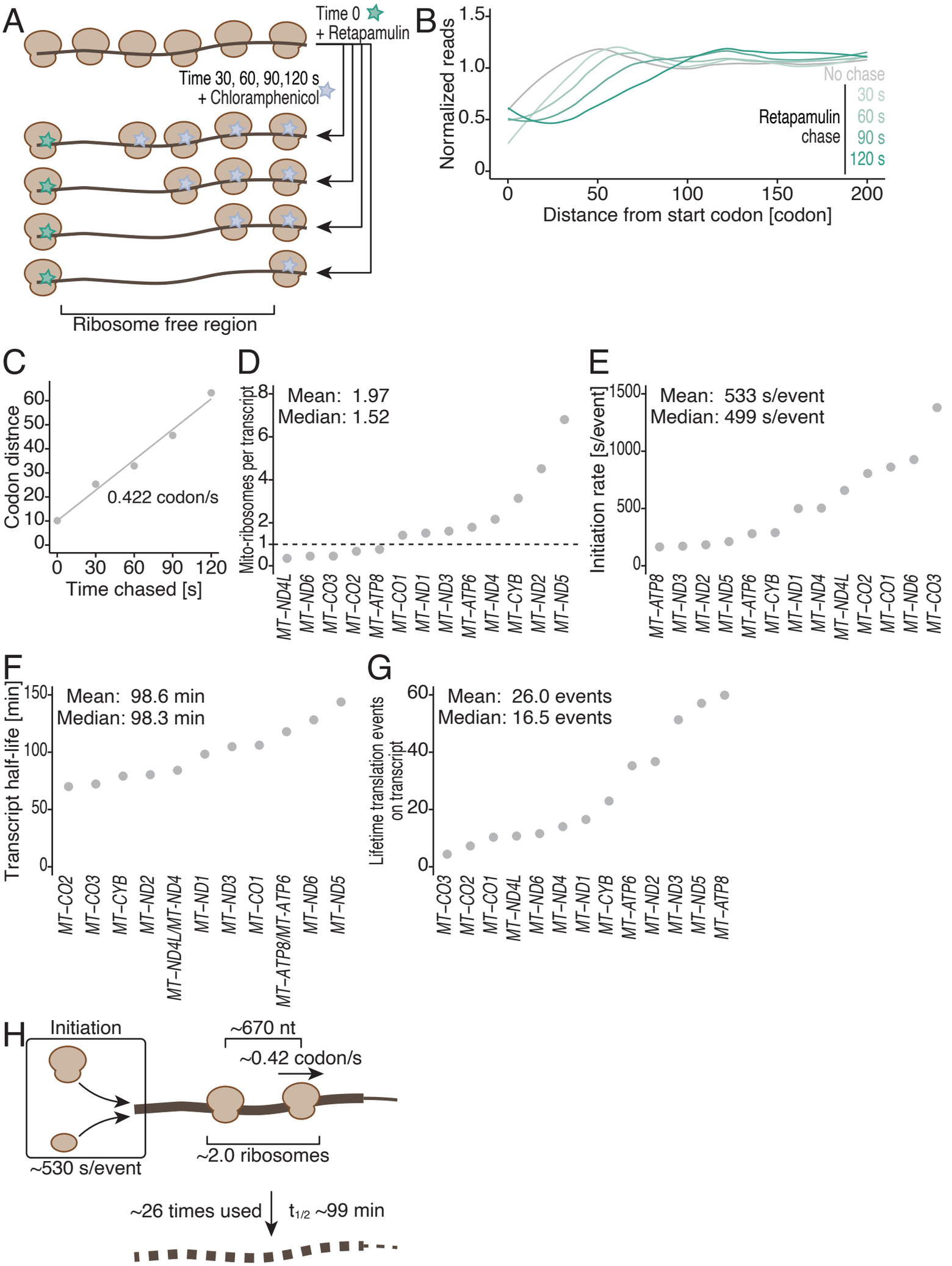

Figure 2 Wakigawa, Mito *et al.* (2023)

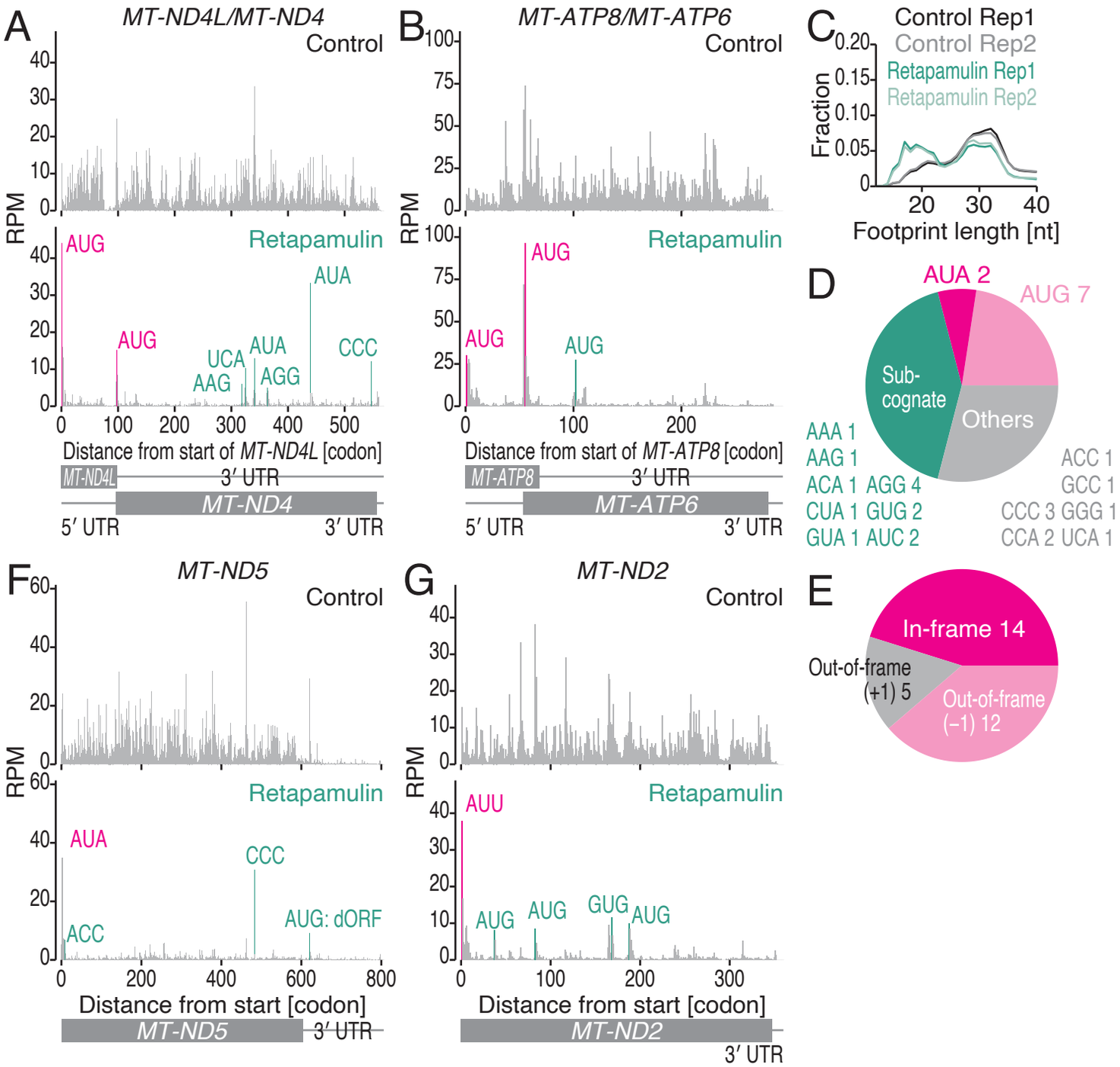

Figure 3 Wakigawa, Mito *et al.* (2023)

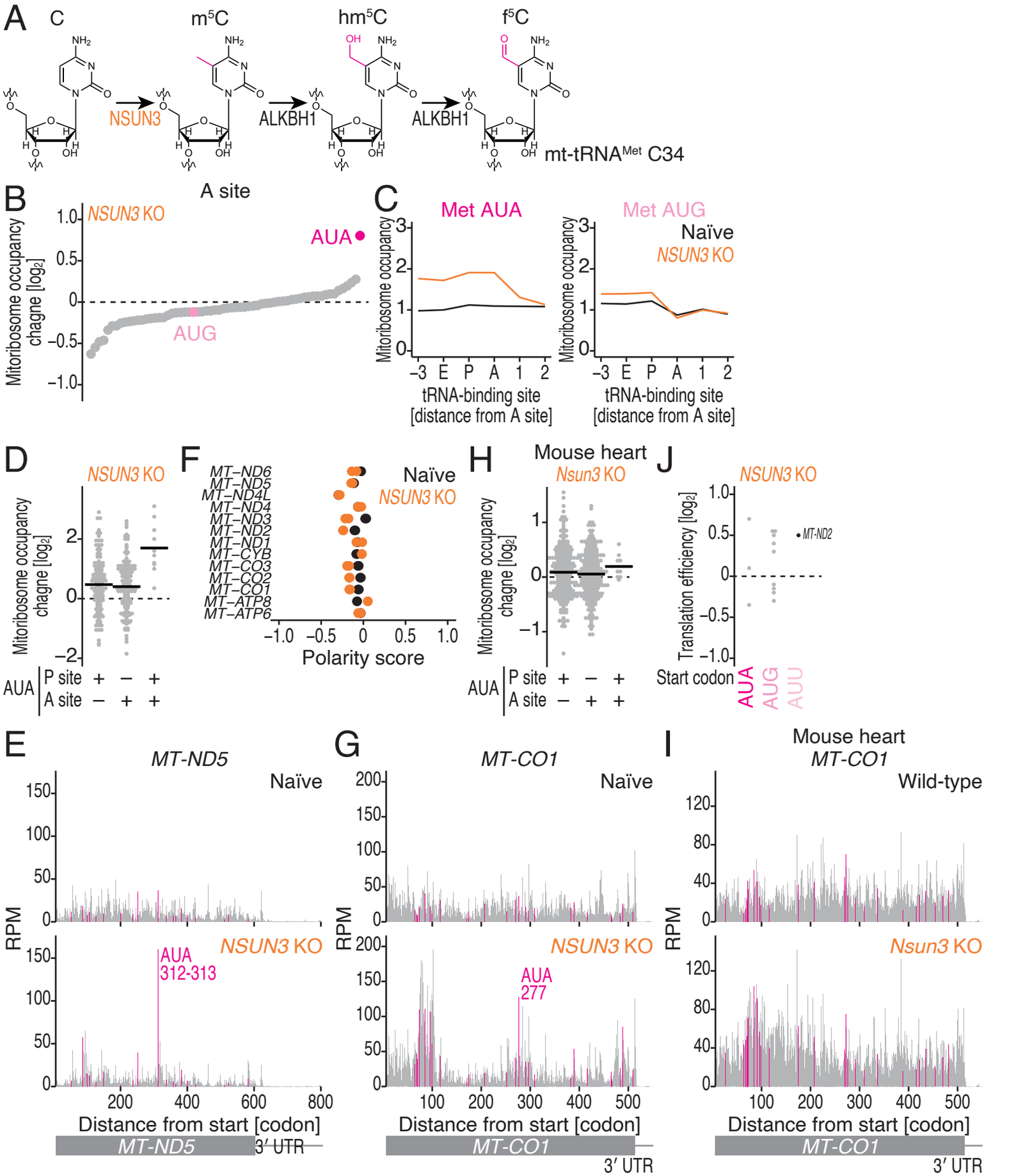

Figure 4 Wakigawa, Mito *et al.* (2023)

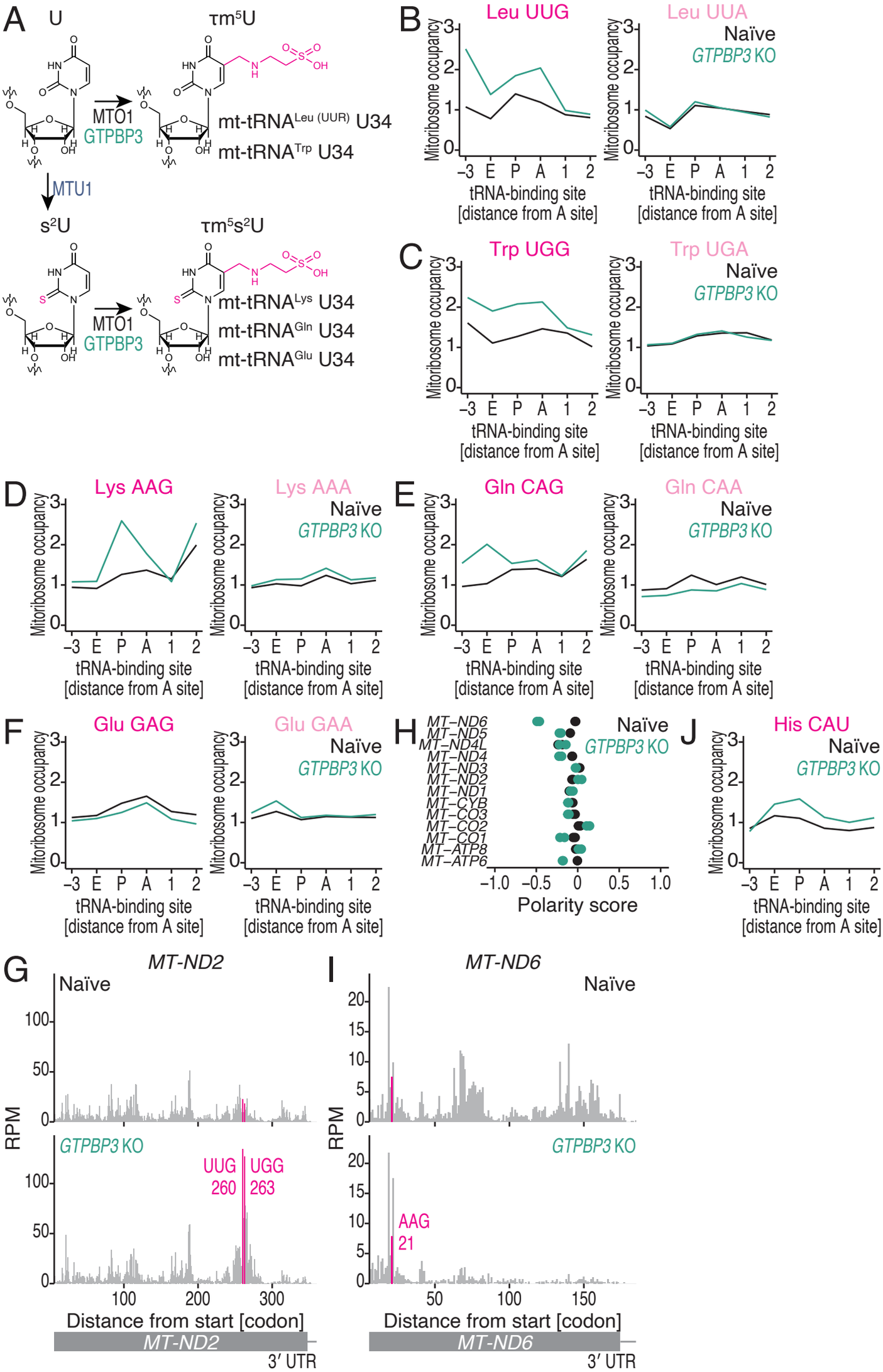

Figure 5 Wakigawa, Mito *et al.* (2023)

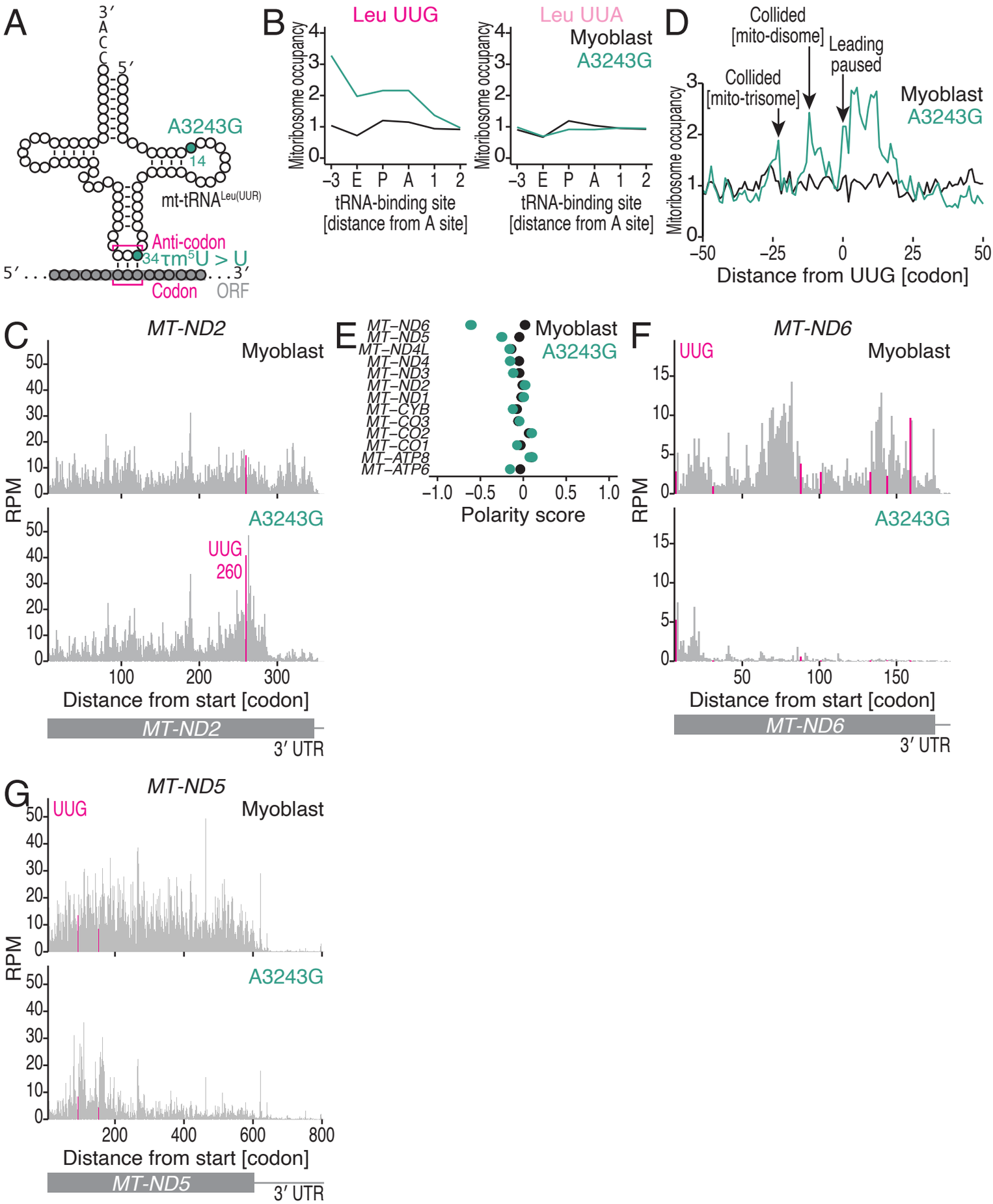

Figure 6 Wakigawa, Mito *et al.* (2023)

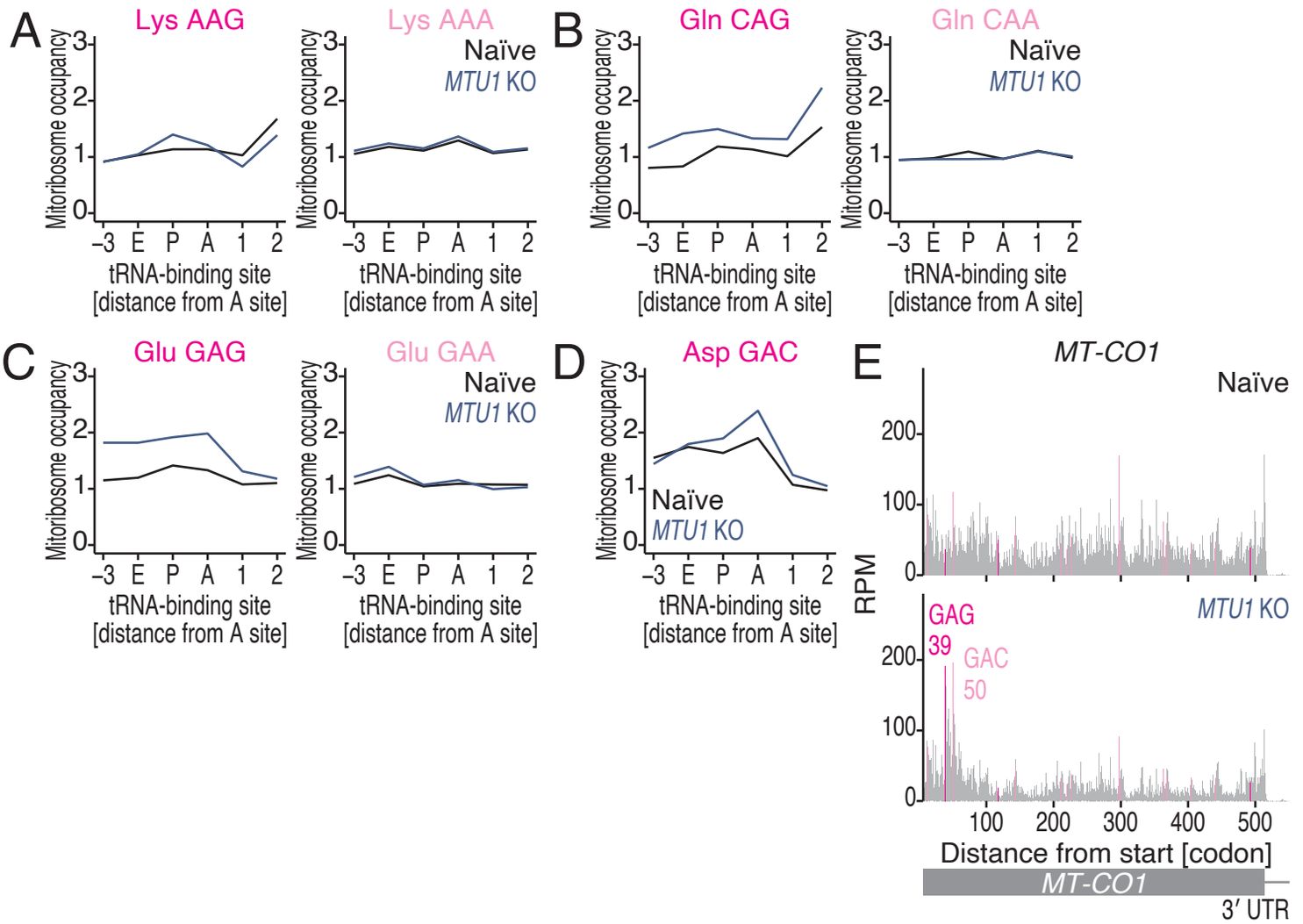

Figure 7 Wakigawa, Mito *et al.* (2023)

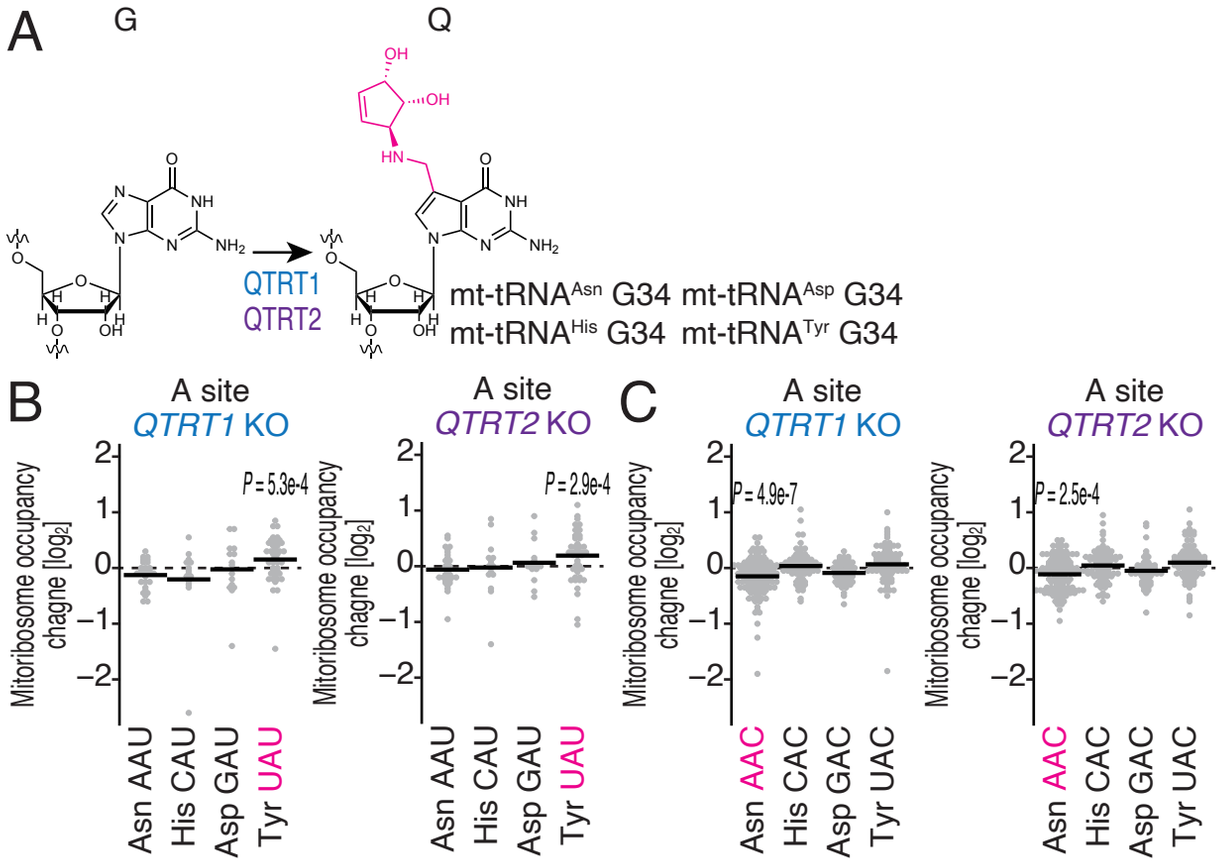

Figure 8 Wakigawa, Mito *et al.* (2023)

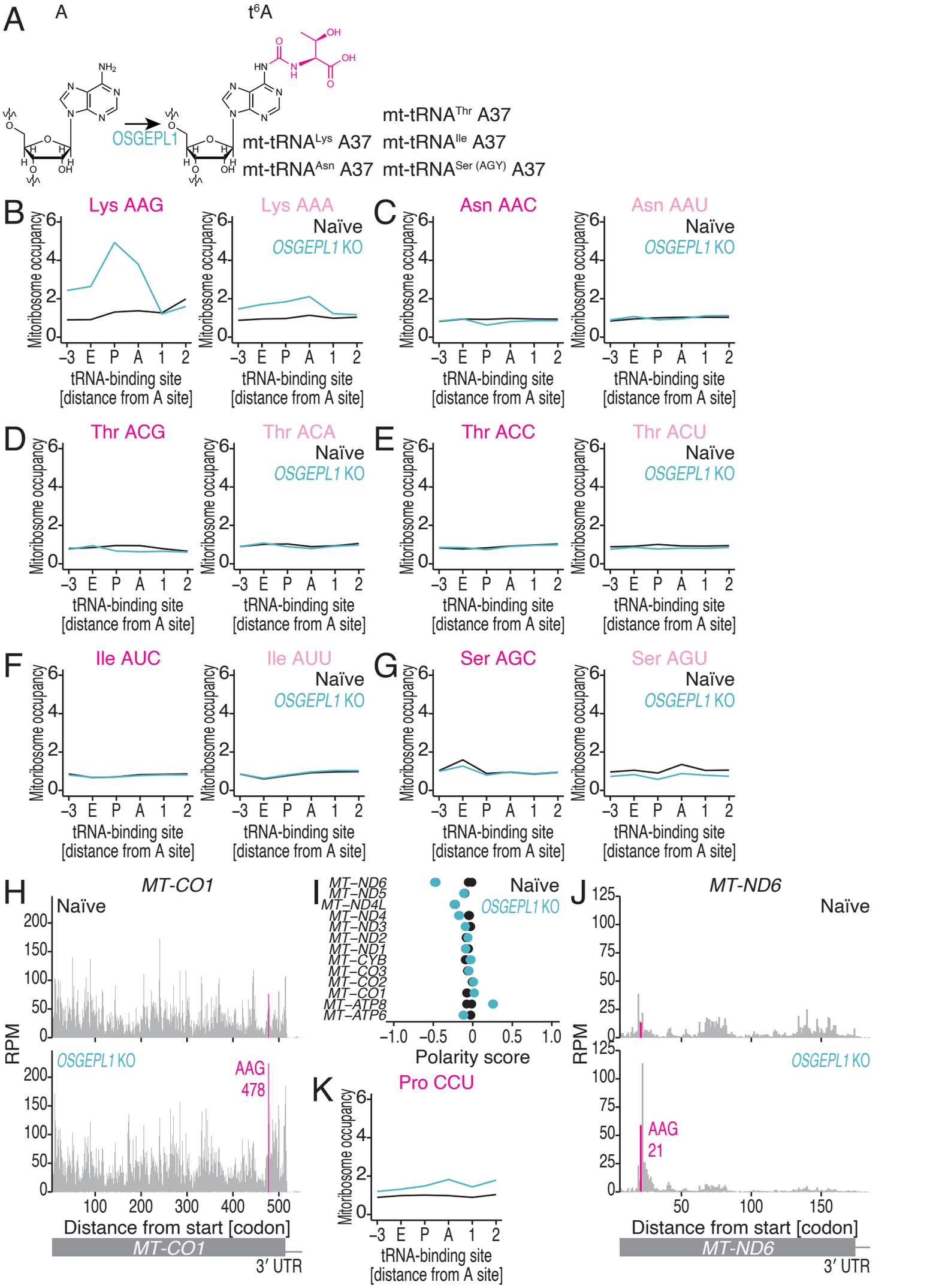

Figure 9 Wakigawa, Mito *et al.* (2023)

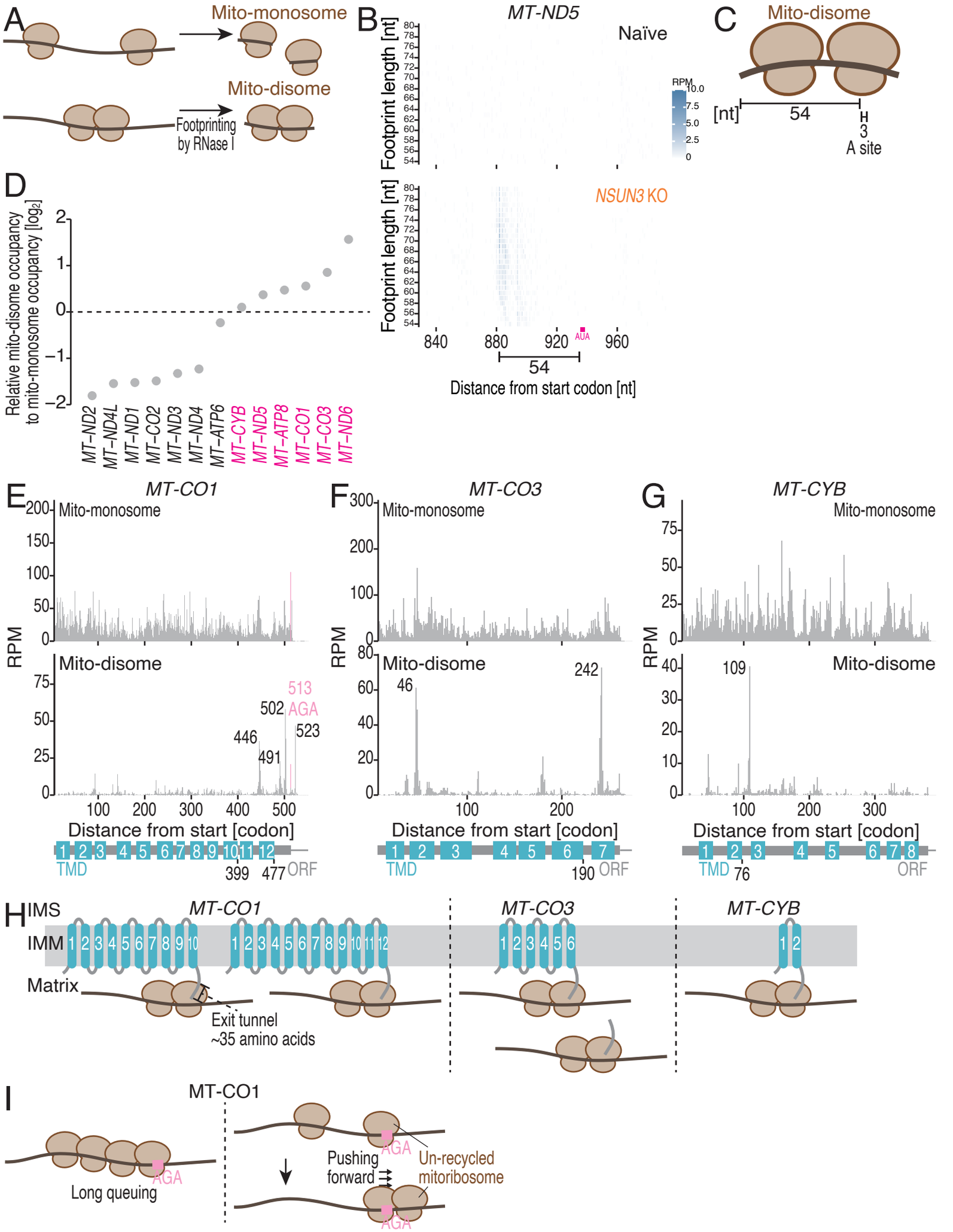

Figure 10 Wakigawa, Mito *et al.* (2023)

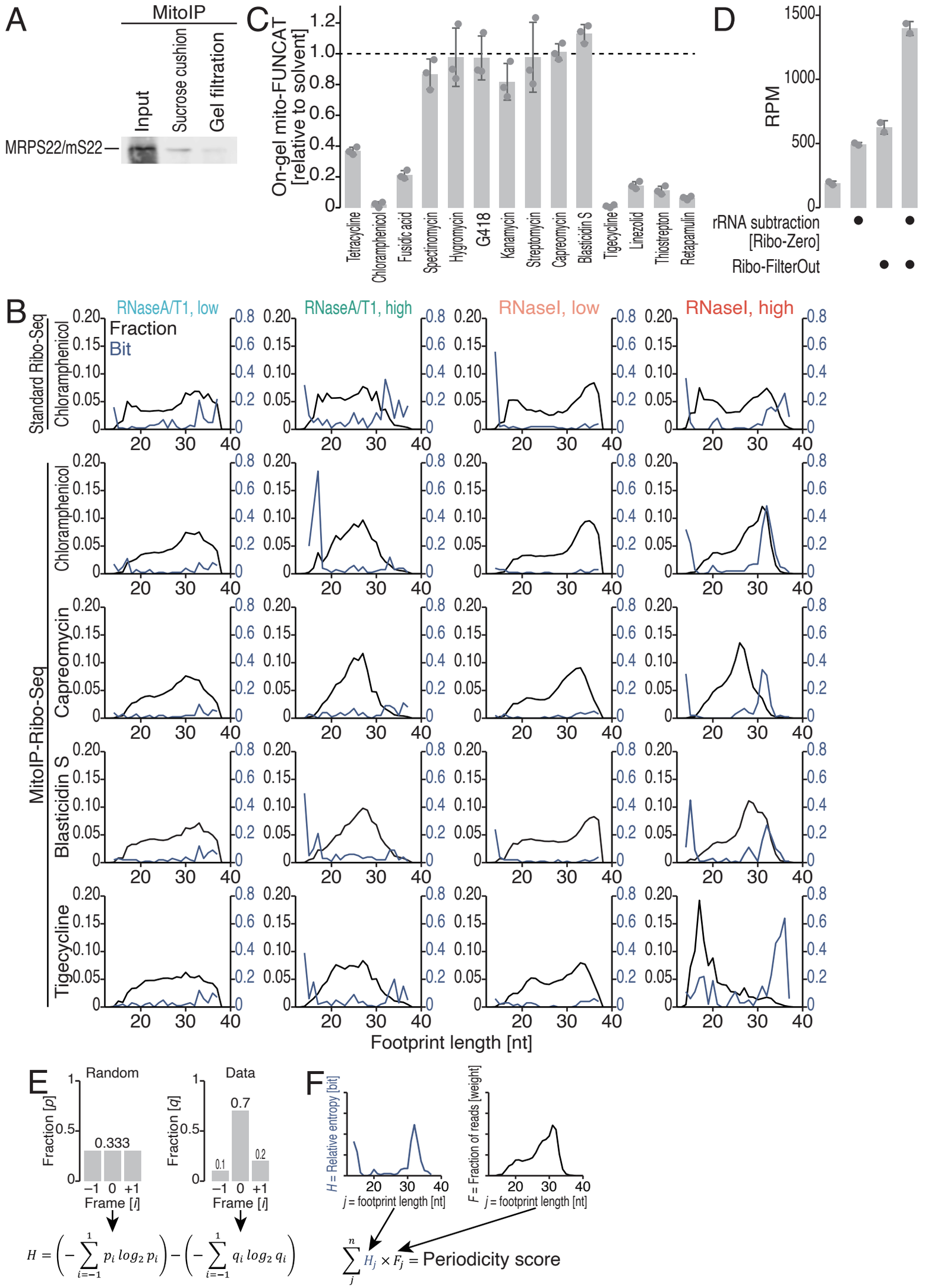

Figure S1 Wakigawa, Mito *et al.* (2023)

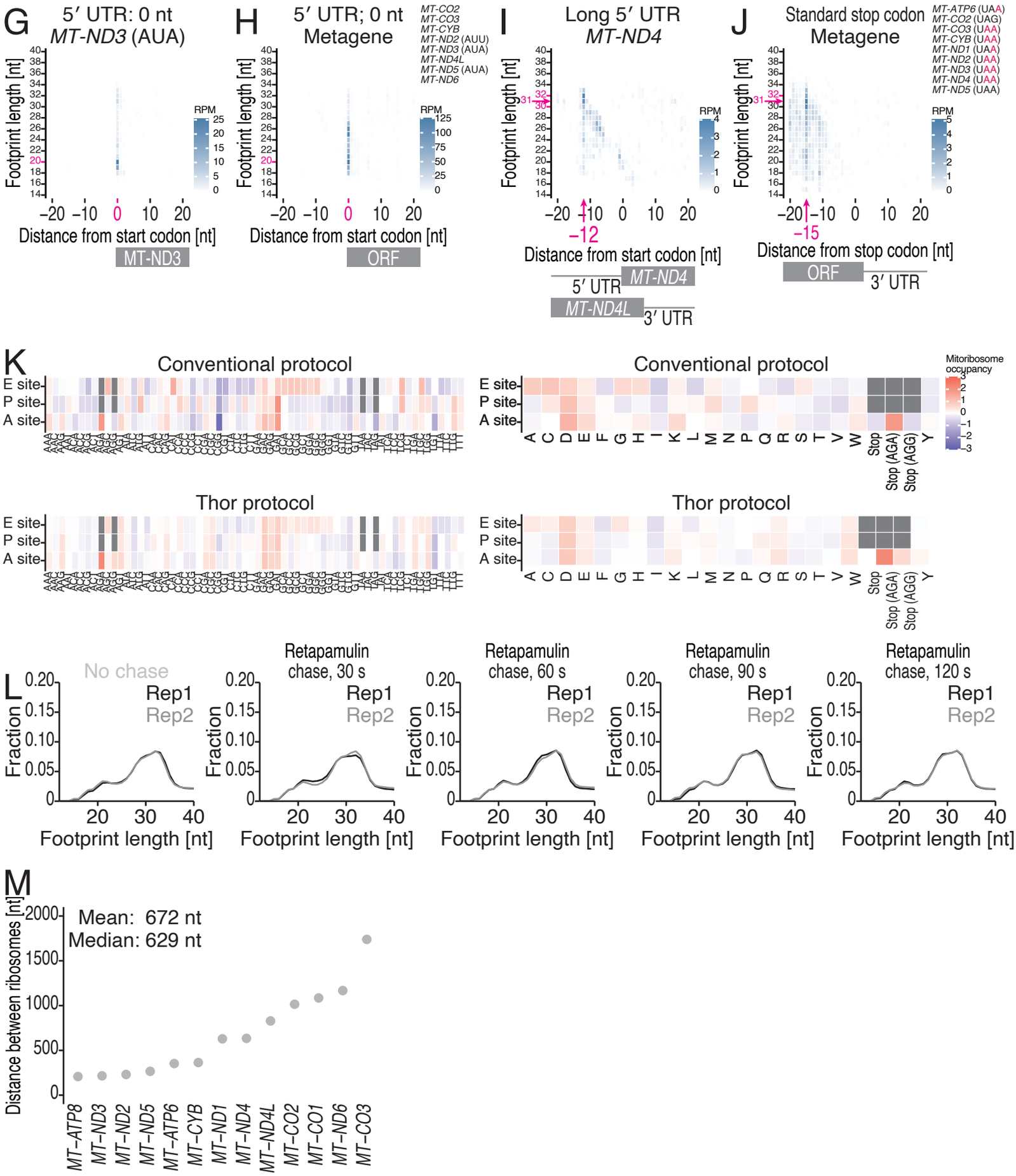

Figure S1 Wakigawa, Mito *et al.* (2023)

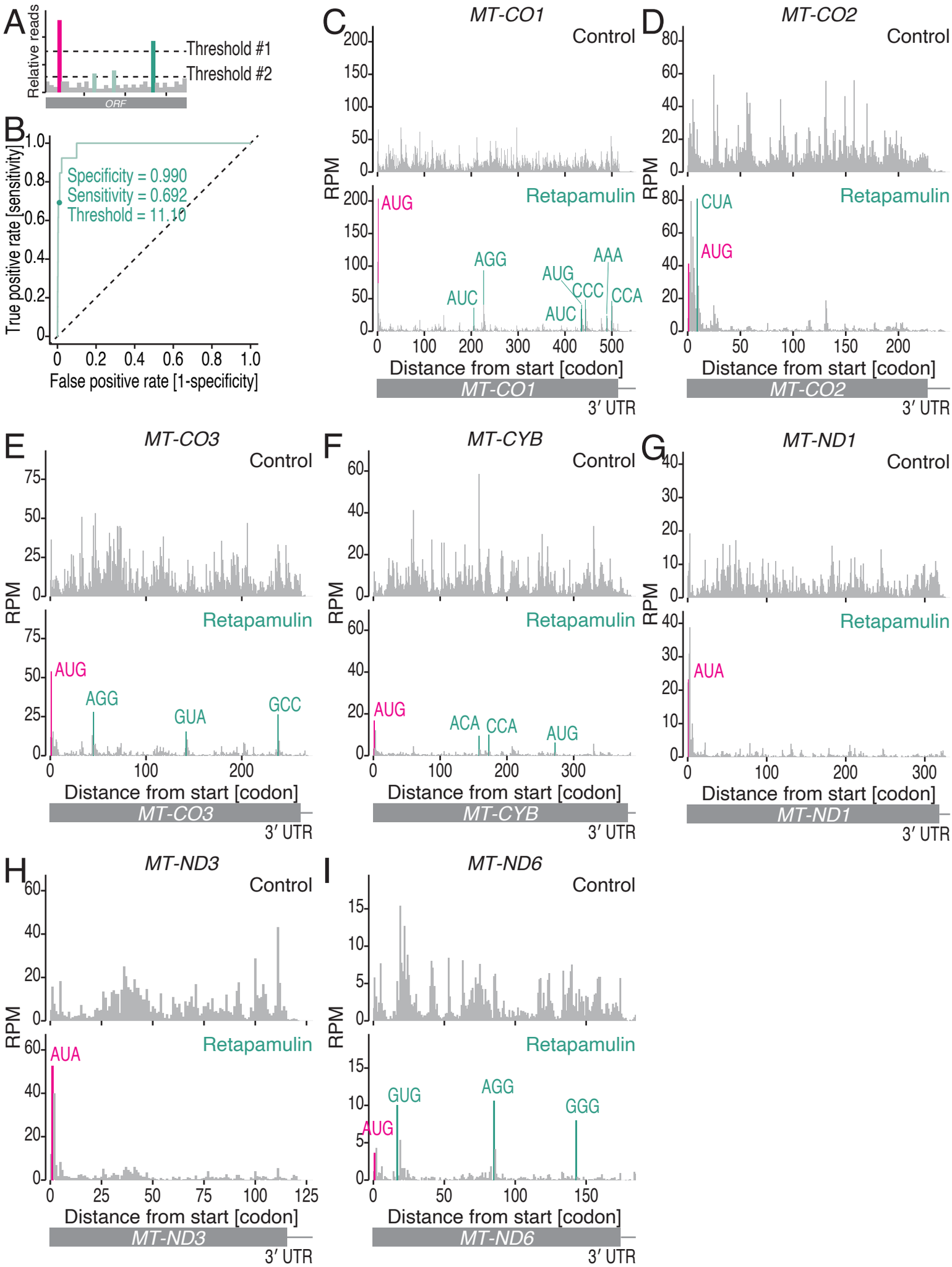

Figure S2 Wakigawa, Mito *et al.* (2023)

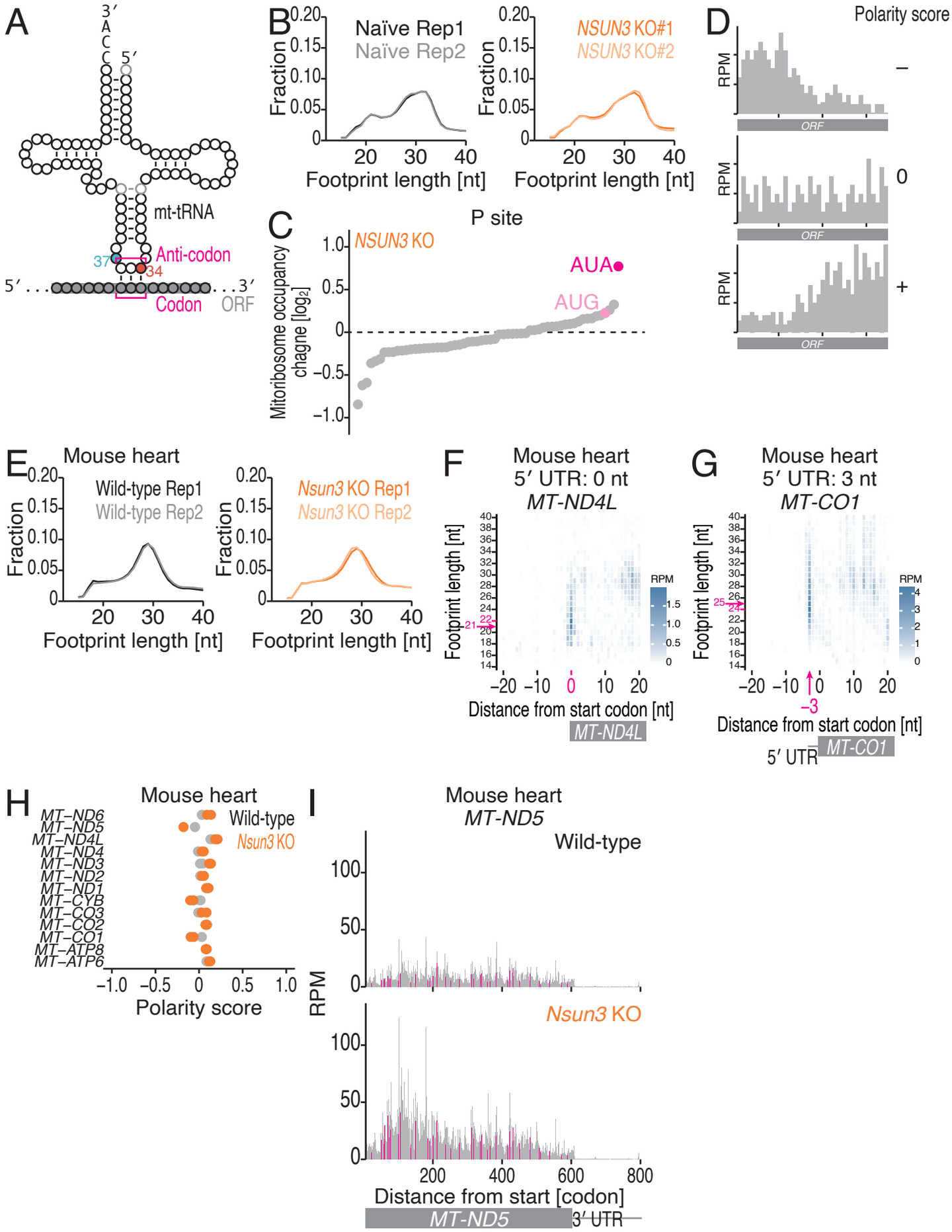

Figure S3 Wakigawa, Mito *et al.* (2023)

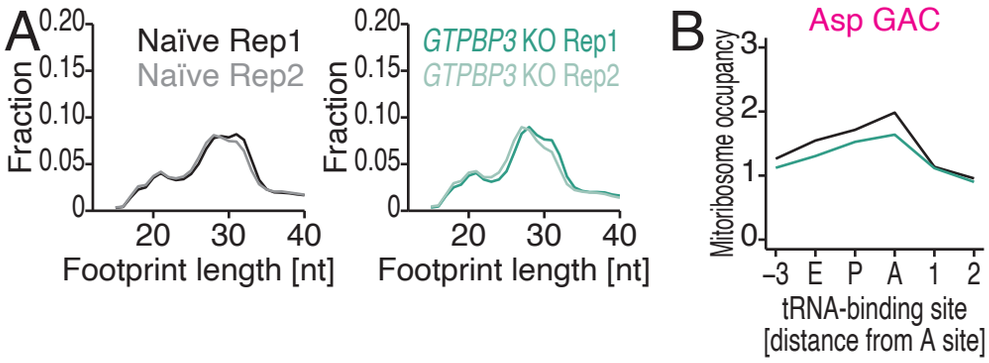

Figure S4 Wakigawa, Mito *et al*. (2023)

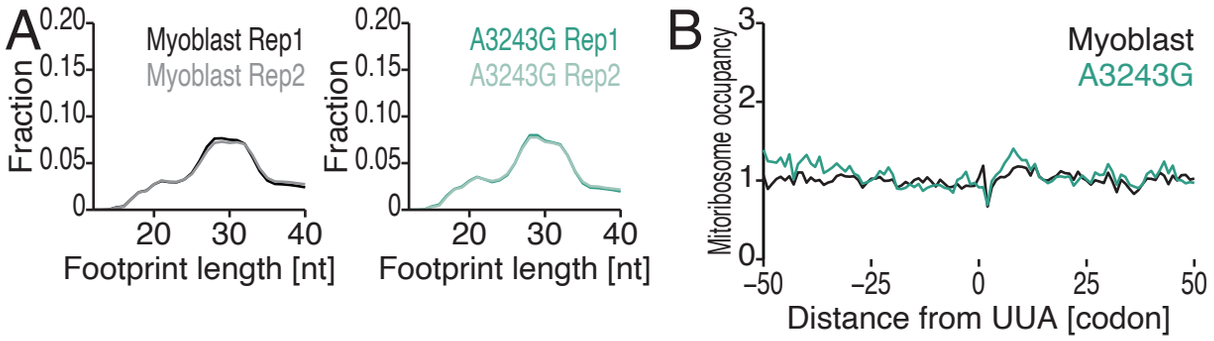

Figure S5 Wakigawa, Mito *et al.* (2023)

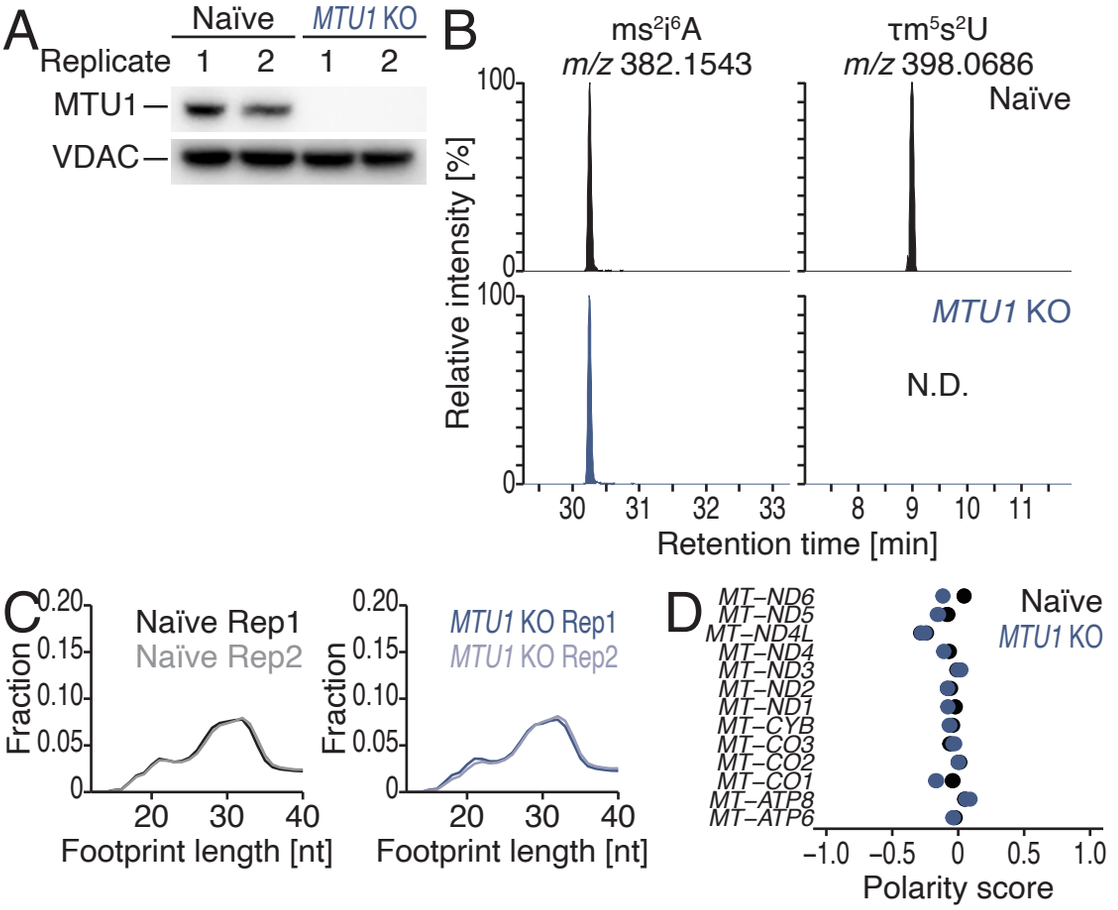

Figure S6 Wakigawa, Mito *et al.* (2023)

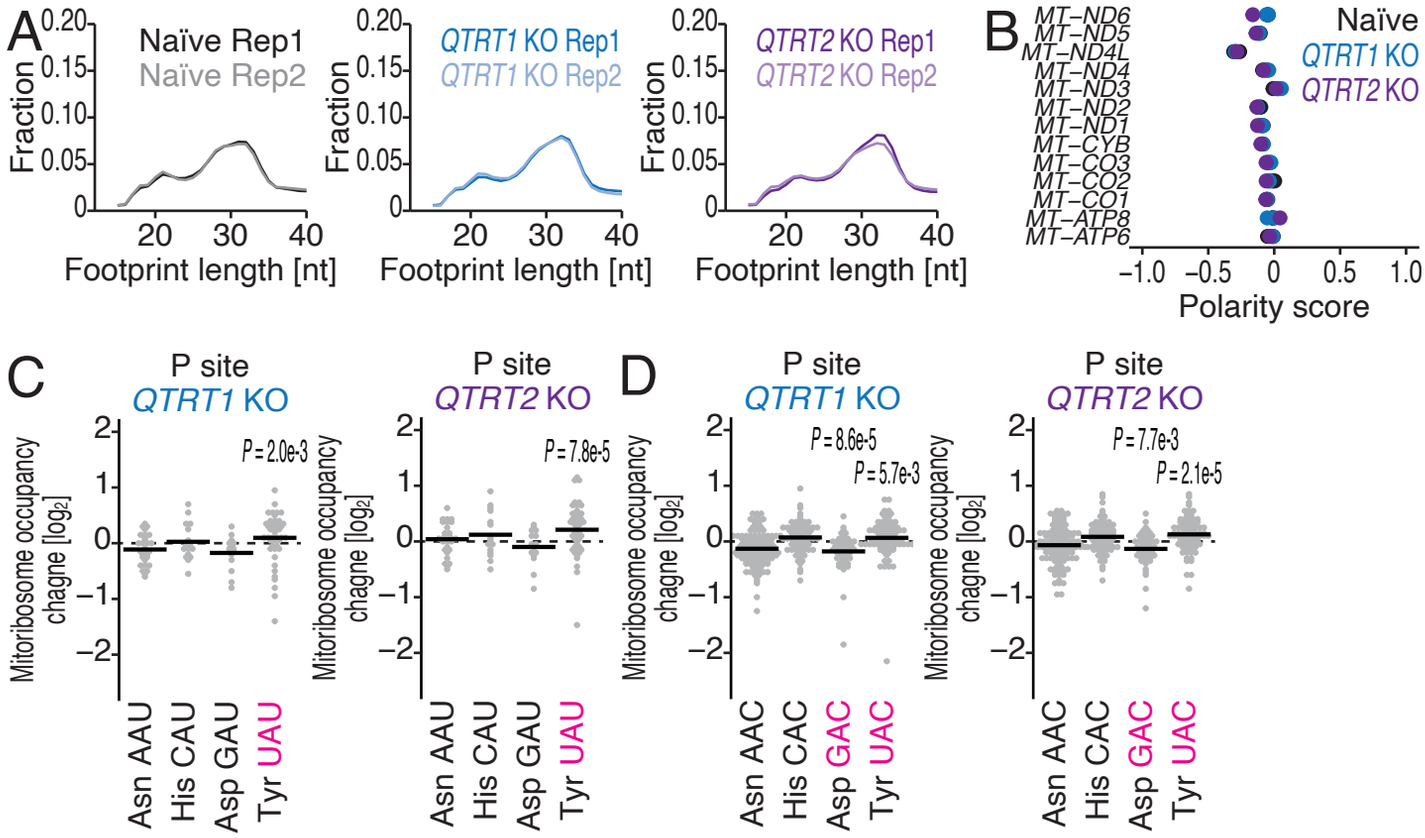

Figure S7 Wakigawa, Mito *et al.* (2023)

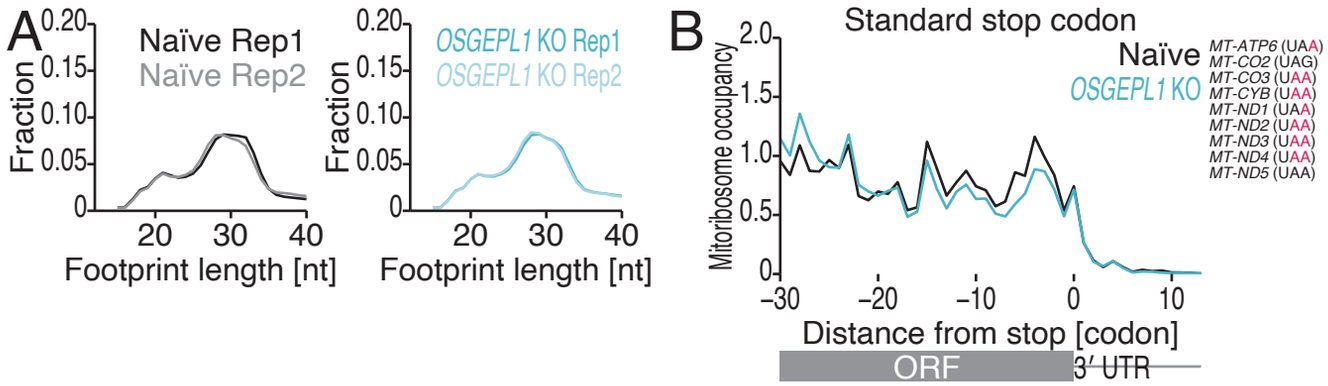

Figure S8 Wakigawa, Mito *et al.* (2023)

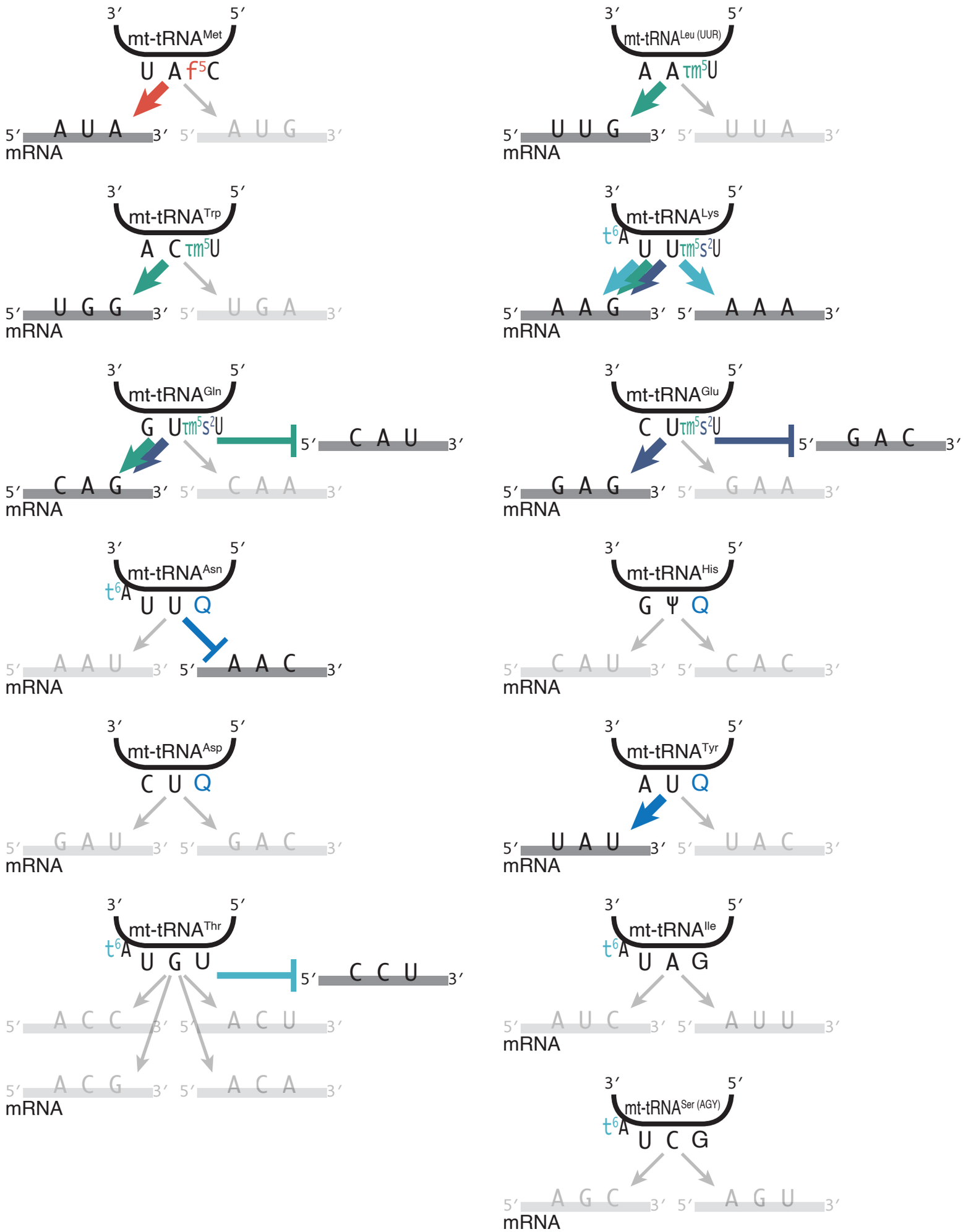

Figure S9 Wakigawa, Mito *et al.* (2023)

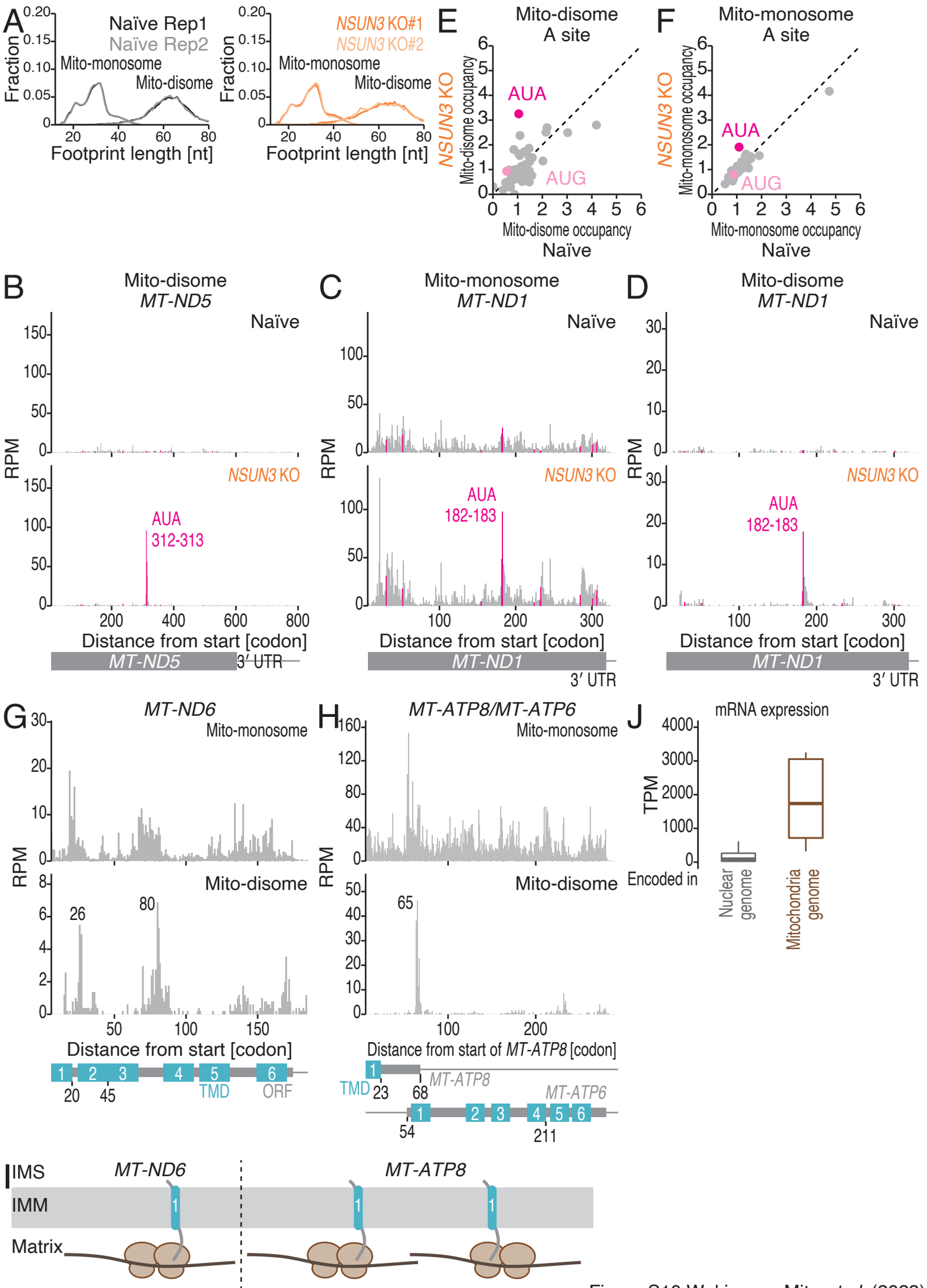

Figure S10 Wakigawa, Mito *et al.* (2023)